

Hierarchical abstraction of weakly coupled synchronized oscillator networks

Jaijeet Roychowdhury^{*,†} and Palak Bhushan

EECS Department, University of California, Berkeley, CA, USA

SUMMARY

We provide a constructive and numerically implementable proof that synchronized groups of coupled, self-sustaining oscillators can be represented as a single effective Perturbation Projection Vector (PPV) (or Phase Response Curve) phase macromodel – in other words, that a group of synchronized oscillators behaves as a single effective oscillator with respect to external influences. This result constitutes a foundation for understanding and predicting synchronization/timing hierarchically in large, complex systems that arise in nature and engineering. We apply this result hierarchically to networks of synchronized oscillators, thereby enabling their efficient and scalable analysis. We illustrate our theory and numerical methods with examples from electronics (networks of three-stage ring oscillators), biology (Fitzhugh–Nagumo neurons) and mechanics (pendulum clocks). Our experiments demonstrate that effective PPVs extracted hierarchically can capture emergent phenomena, such as pattern formation, in coupled oscillator networks. Copyright © 2015 John Wiley & Sons, Ltd.

Received 8 April 2014; Revised 13 August 2014; Accepted 14 August 2014

KEY WORDS: coupled oscillators; synchronization; injection locking; model reduction; PPV; PRC; phase macromodels; hierarchy

1. INTRODUCTION

Coupled oscillator networks (CONs, Figure 3) arise in diverse fields, including electronics, biology and mechanics. As the name suggests, such networks comprised individual self-sustaining oscillators [1–3] that interact, often only slightly, via non-oscillatory mechanisms. CONs are capable of exhibiting quite intriguing global dynamics, even if interactions between individual oscillators are purely local in nature. In particular, the phenomenon of *synchronization*, in which oscillators in the entire network become phase locked to each other (via the phenomenon of injection locking [4, 5]), has long been known and has attracted much attention[‡]. Examples in nature and biology include the synchronized flashing of fireflies [9], synchronization in the heart's pacemaking system [10] and circadian rhythms in which virtually every cell in an organism becomes synchronized to the rising and setting of the sun [11]. Synchronization in CONs occurs also in electric power grids [12], on-chip electronic clock distribution networks [13, 14], microwave phased-array antenna grids, systems of interacting mechanical pendulums [15, 16] and so on (Figure 1). A visually appealing synchronization-related phenomenon in CONs is that of spatio-temporal pattern formation, for example, in biochemical systems [17–19]. Such pattern formation has been studied using reaction diffusion theory [20] using CON representations, for example, of the Brusselator and Belousov–Zhabotinsky reaction diffusion systems [19, 21–27].

^{*}Correspondence to: Jaijeet Roychowdhury, EECS Department, University of California, Berkeley, CA, USA.

[†]E-mail: jr@berkeley.edu

[‡]Synchronization is not, by any means, the only phenomenon of interest in CONs; other effects such as pulling [6], quasi-periodicity [7] and chaos [8] can be manifested. This work focusses only on fully synchronized networks.

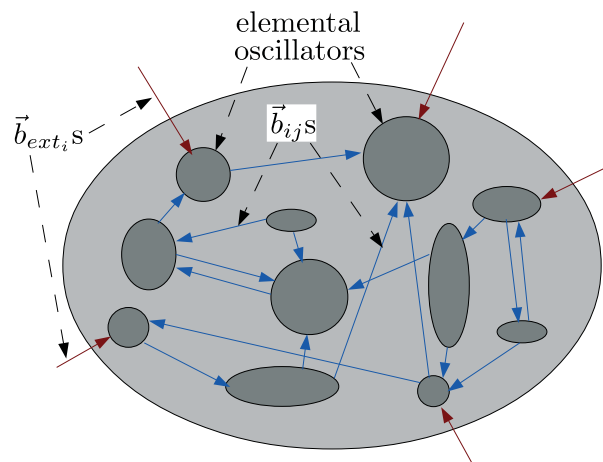


Figure 1. A generic network of coupled elemental oscillators. The light gray ellipse represents the network abstracted as a single equivalent Perturbation Projection Vector model.

In seminal work, Winfree [28] developed and applied the concept of oscillator Phase Response Curves (PRCs) to analyse weakly coupled CONs with nearly identical oscillators, demonstrating analytically that the system will lock if the spread of the oscillators is small enough. The well-known model of Kuramoto [29, 30] simplified Winfree's model considerably to identical, purely sinusoidal couplings between oscillators with sinusoidal PRCs for further analytical tractability. Bohn *et al.* [31] used the Kuramoto model to explore the effects of local versus global coupling on spatio-temporal pattern formation; however, Lai and Roychowdhury [32] demonstrated that approximating non-sinusoidal PRCs as sinusoidal, as the Kuramoto model does, can lead to qualitatively wrong pattern predictions. A detailed review of the theoretical evolution of the field can be found in [33]; virtually, all treatments to date require simplifying assumptions about network coupling and/or the oscillators themselves for the sake of analytical tractability [34].

In spite of the body of work available on CONs, detailed and precise analysis remains a significant challenge; indeed, even for a single oscillator, no closed form expressions for, for example, injection locking response are available in general, and analytical approaches typically need to be complemented by numerical techniques [5, 35]. Moreover, collective behaviour tends to manifest itself only after a CON exceeds a certain characteristic size, which makes simplifications for analytical tractability (typically valid only for small CON sizes) inapplicable to the point that qualitatively wrong predictions result [36, 37].

Computational methods are thus an important component of the toolbox for analysing CONs, as they are for many complex engineering and natural systems (e.g. SPICE [38] for designing circuits). Computational analysis of oscillatory systems faces unique challenges, however, that stem from the fundamental marginal phase stability of any self-sustaining oscillator [39, 40]. Phase errors resulting from numerical solution of differential equations accumulate without bound, forcing the use of very small timesteps to control error accumulation, especially for stiff systems [41, 42]. As a result, direct simulation of CONs, in which each oscillator is modelled using a multi-dimensional set of autonomous differential equations with external inputs, can be computationally prohibitive.

It is possible, however, to abstract the *phase dynamics* of any self-sustaining, orbitally stable [43] oscillator as a *single, scalar differential equation*, termed a PRC or Perturbation Projection Vector (PPV) (macro)model [28, 39, 44]. Despite being an approximation[§], the PPV model of an oscillator

[§]Valid, in theory, only for small perturbing inputs to the oscillator; more precisely, small perturbations in the limit cycle due to the perturbation are ignored; only the perturbations to the phase are retained.

can in fact produce more accurate numerical results than the original differential equations, and with greater computational efficiency, because the abstraction process removes stiffness, enabling higher-order integration techniques to be applied to the PPV model. Indeed, PPV models have been shown to capture synchronization and emergent phenomena accurately in large networks of coupled oscillators [32, 45]. For oscillators whose autonomous differential equation systems are large (e.g. of size ~ 100 for certain cellular circadian oscillators, and in the thousands for many on-chip electronic oscillators), the reduction in size offered by the PPV model can result in substantial computational speedup [32].

In this work, we extend the concept of PPV/PRC models to apply not only to individual oscillators but also to groups of coupled oscillators that are synchronized. Specifically, we show that if a group of oscillators, each represented by a PPV model, becomes phase synchronized, then its phase dynamics as a whole (with respect to perturbations external to the group) can be captured with a *single effective group PPV model* [46]. Our proof of this fact is constructive and numerically implementable.

An important implication of this result is that it becomes possible to analyse and understand the dynamics of CONs *hierarchically*. In many large networks of interacting oscillators, sub-groups exist that are, for example, more tightly coupled to each other than to the rest of the network – for example, central pattern generator models for locomotion in *C. Elegans* [47], leeches [48] and many other creatures. Our aforementioned result provides a concrete foundation for regarding each of these sub-groups, if synchronized to each other, effectively as a *single oscillator*.

Indeed, it has long been an empirical practice for groups of oscillators to be thought of, and modelled, as single oscillators. For example, in spintronics, models of ‘individual’ spin-torque oscillators often really represent the synchronized interaction of many underlying spin domains [49]. In the study of circadian rhythms, it is the norm to regard an entire organism (such as a rat, or a human being) as a single circadian oscillator that responds to light, and to measure its PRCs experimentally [50]. Because our result applies to any synchronized network of PPV models, whether they are of individual oscillators or synchronized groups, it can be repeatedly applied to hierarchically grouped sets of synchronized oscillators to obtain, if desired, a single effective oscillator model for all the oscillators in the network. To our knowledge, this result provides the first mathematically sound basis for the group-oscillator assumptions and models seen in the literature. Moreover, it provides concrete techniques for deriving the characteristics of such effective group oscillators precisely in the form of PRC/PPV models, thereby constituting a bottom-up way of understanding the dynamics and synchronization of complex, non-uniform networks of oscillators quantitatively. Unlike past work (such as [51], which assumes perfectly identical oscillators and uniform coupling), our result and abstraction technique makes no assumptions about the network (beyond those inherent in the PRC/PPV model [28, 39]) – that is, it applies to completely heterogeneous networks of arbitrary oscillators and network coupling.

Hierarchical analysis of large networks of coupled oscillators also confers computational advantages, because only small groups of lower-level models need be analysed for locking. In arbitrary, non-uniform networks of N oscillators (whether sparsely or densely connected), exploiting hierarchy leads to $O(N)$ computational speedup. The speedups are greater if symmetry or uniformity is present in parts of the network.

We demonstrate our theory and hierarchical numerical abstraction technique on grids of coupled electrical ring oscillators, Fitzhugh–Nagumo neuronal oscillators [2] and mechanical pendulum clocks. We show that despite the approximations inherent in abstraction, higher-level networks of group PPVs successfully predict emergent patterns. We obtain speedups of 10–100 \times (in a MATLAB implementation) by exploiting hierarchy.

The remainder of the paper is organized as follows. In Section 2, we provide a brief review of PRC/PPV phase models for oscillators and set the stage for Section 3, in which we prove that synchronized groups of coupled oscillators can be abstracted using a single effective PPV model. In Section 4, we demonstrate our technique on networks of electronic, biological and mechanical oscillators and provide additional numerical details.

2. PRELIMINARIES: PRC/PPV PHASE MACROMODELS

Given an ODE or DAE description

$$\frac{d}{dt}\vec{q}(\vec{x}(t)) + \vec{f}(\vec{x}) + \vec{b}(t) = \vec{0} \quad (1)$$

of an oscillator with an orbitally stable T -periodic autonomous solution $\vec{x}_s(t)$, it can be shown [39, 52] that the timing jitter or phase characteristics of the oscillator, under the influence of small perturbations $\vec{b}(t)$, can be captured by the nonlinear scalar differential equation

$$\frac{d}{dt}\alpha(t) = \vec{v}_1^T(t + \alpha(t))\vec{b}(t), \quad (2)$$

where the quantity $\vec{v}_1(\cdot)$, a T -periodic function of time, is known as the PRC [28] or PPV [39, 44].

For convenience, we scale the time axis to normalize all periods to 1. Define a one-periodic version of the steady state solution to be

$$\vec{x}_p(t) = \vec{x}_s(tT), \quad (3)$$

and a one-periodic version of the PPV to be

$$\vec{p}(t) = \vec{v}_1(tT). \quad (4)$$

Using these one-periodic quantities and defining $f \triangleq \frac{1}{T}$, (2) can be expressed as

$$\frac{d}{dt}\alpha(t) = \vec{p}^T(ft + f\alpha(t))\vec{b}(t). \quad (5)$$

Defining *phase* to be

$$\phi(t) = ft + f\alpha(t), \quad (6)$$

(5) becomes

$$\frac{d}{dt}\phi(t) = f + f\vec{p}^T(\phi(t))\vec{b}(t). \quad (7)$$

$x(t)$, the solution of (1), can often be approximated usefully by a phase-shifted version of its unperturbed periodic solution, that is,

$$\vec{x}(t) \simeq \vec{x}_s(T\phi(t)) = \vec{x}_p(\phi(t)). \quad (8)$$

(2) (or equivalently (7)) is termed the *PPV equation* or *PPV phase macromodel*. In the absence of any perturbation $\vec{b}(t)$, note that $\alpha(t) \equiv 0$ (w.l.o.g), $\vec{x}(t) = \vec{x}_s(t) = \vec{x}_p(ft)$ and $\phi(t) = ft$. We will call the latter the *phase of natural oscillation* and denote it by $\phi^\diamond(t) \triangleq ft$.

3. MAIN THEORY: DERIVATION OF HIERARCHICAL PPV MACROMODEL

3.1. Coupled phase system and its properties

3.1.1. Coupled system of PPV phase macromodels. Consider a group of $N \geq 2$ coupled oscillators (Figure 2). We model each oscillator by its PPV Equation (7):

$$\frac{d}{dt}\phi_i(t) = f_i + f_i\vec{p}_i^T(\phi_i(t))\vec{b}_i(t), \quad i = 1, \dots, N, \quad (9)$$

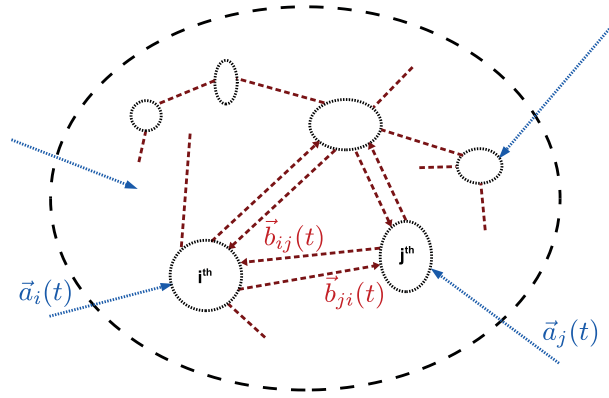


Figure 2. Oscillator system with internal coupling and external inputs.

where i -subscripted quantities refer to the i^{th} oscillator. Inputs to each oscillator are drawn from two sources (as depicted in Figure 2): (1) internal couplings with other oscillators and (2) external sources. $\vec{b}_i(t)$ can therefore be written as

$$\vec{b}_i(t) = \vec{a}_i(t) + \sum_{\substack{j=1 \\ j \neq i}}^N \vec{b}_{ij}(\phi_j(t)), \quad (10)$$

where $\vec{a}_i(t)$ is the external input (i.e. from outside the group of N oscillators) to the i^{th} oscillator, and $\vec{b}_{ij}(\phi_j(t))$ represents the influence of the j^{th} oscillator on the i^{th} .

We make the natural assumption that the $\vec{b}_{ij}(\cdot)$ are one-periodic – that is, that each oscillator generates outputs that follow its own phase and timing properties; it is these outputs that couple internally to the inputs of other oscillators. Note that as i varies, the dimensions of $\vec{p}_i(t)$, $\vec{a}_i(t)$ and \vec{b}_{ij} can differ, because they depend on the size of the i^{th} oscillator's differential equations.

The system of N equations (9) can be written in vector ODE form as

$$\frac{d}{dt} \vec{\phi}(t) = \vec{g}_{\phi}(\vec{\phi}(t)) + \vec{b}_{\phi}(\vec{\phi}(t), t), \quad (11)$$

where

$$\vec{\phi}(t) \triangleq \begin{bmatrix} \phi_1(t) \\ \vdots \\ \phi_N(t) \end{bmatrix}, \quad (12)$$

$$\vec{g}_{\phi}(\vec{\phi}) \triangleq \begin{bmatrix} f_1 + f_1 \vec{p}_1^T(\phi_1) \sum_{j=2}^N \vec{b}_{1j}(\phi_j(t)) \\ \vdots \\ f_N + f_N \vec{p}_N^T(\phi_N) \sum_{j=1}^{N-1} \vec{b}_{Nj}(\phi_j(t)) \end{bmatrix}, \quad (13)$$

$$\text{and } \vec{b}_{\phi}(\vec{\phi}, t) \triangleq \begin{bmatrix} f_1 \vec{p}_1^T(\phi_1) \vec{a}_1(t) \\ \vdots \\ f_N \vec{p}_N^T(\phi_N) \vec{a}_N(t) \end{bmatrix} = \begin{bmatrix} f_1 \vec{p}_1^T(\phi_1) & 0 & 0 & \dots & 0 & 0 \\ & \ddots & & & & \\ 0 & 0 & \dots & 0 & 0 & f_N \vec{p}_N^T(\phi_N) \end{bmatrix} \begin{bmatrix} \vec{a}_1(t) \\ \vdots \\ \vec{a}_N(t) \end{bmatrix} = B_{\phi}(\vec{\phi}) \vec{a}(t). \quad (14)$$

We will refer to (11) as the *Coupled Phase System (CPS)*.

Note that $\vec{b}_\phi(\vec{\phi}, t) \equiv \vec{0}$ in the absence of inputs external to the group of oscillators, that is, when $a_i(t) \equiv \vec{0}$. Note also that $\vec{g}_\phi(\vec{\phi})$ is one-periodic in each component of $\vec{\phi}$, that is, it is one-periodic in each ϕ_i . Such functions are termed *cylindrical* [43, page 236].

3.1.2. Locking in the absence of external inputs.

Assumption 3.1

In the absence of external inputs (i.e. if $\vec{a}_i(t) \equiv \vec{0}$, $\forall i$), assume that the group of N oscillators locks stably[¶] to a common frequency f^* (equivalently, with a common period $T^* = \frac{1}{f^*}$).

Denote the phase of the i^{th} oscillator, when locked as in Assumption 3.1 to the other oscillators in the group, by $\phi_i^*(t)$. Note that this phase will typically be different from the oscillator's phase of natural oscillation $\phi_i^\diamond(t) = f_i t$, on account of inputs via coupling from other oscillators in the group.

Denoting

$$\vec{\phi}^*(t) \triangleq \begin{bmatrix} \phi_1^*(t) \\ \vdots \\ \phi_N^*(t) \end{bmatrix}, \quad (15)$$

note that $\vec{\phi}^*(t)$ satisfies (11) with no external inputs, that is,

$$\frac{d}{dt} \vec{\phi}^*(t) = \vec{g}_\phi(\vec{\phi}^*(t)). \quad (16)$$

We term $\vec{\phi}^*(t)$ the *system phase during externally unperturbed lock*.

3.1.3. *D-periodicity of $\vec{\phi}^*(t)$.* T^* -periodicity of each oscillator locked at frequency f^* implies that

$$\vec{x}_i(t) = \vec{x}_{p,i}(\phi_i^*(t)) \quad (17)$$

is T^* -periodic $\forall i$; that is,

$$\begin{aligned} \vec{x}_i(t + T^*) &= \vec{x}_i(t), \quad \text{or} \\ \vec{x}_{p,i}(\phi_i^*(t + T^*)) &= \vec{x}_{p,i}(\phi_i^*(t)). \end{aligned} \quad (18)$$

From definition, $\vec{x}_{p,i}(\cdot)$ is one-periodic. Equation (18) is satisfied for *arbitrary* one-periodic $\vec{x}_{p,i}(\cdot)$ iff

$$\phi_i^*(t + T^*) = n + \phi_i^*(t), \quad \forall t, \quad n \in \mathbb{Z}. \quad (19)$$

Define the *ideal phase of oscillation at frequency f^** to be

$$\phi_{\text{ideal}}^*(t) = f^* t. \quad (20)$$

$\phi_{\text{ideal}}^*(t)$ satisfies (19) (with $n = 1$), but note that the phase of each locked oscillator in the system need not necessarily equal $\phi_{\text{ideal}}^*(t)$. A more general form for $\phi_i^*(t)$ that also satisfies (19) is

$$\phi_i^*(t) = \phi_{\text{ideal}}^*(t) + \Delta\phi_i^*(t) = f^* t + \Delta\phi_i^*(t), \quad (21)$$

[¶]Section 3.5 will expand on the notion of lock stability.

where $\Delta\phi_i^*(t)$ is itself T^* -periodic^{||}. Equivalently^{**},

$$\vec{\phi}^*(t) = \phi_{\text{ideal}}^*(t) + \overrightarrow{\Delta\phi}^*(t) = f^*t + \overrightarrow{\Delta\phi}^*(t), \quad (22)$$

where

$$\overrightarrow{\Delta\phi}^*(t) \triangleq \begin{bmatrix} \Delta\phi_1^*(t) \\ \vdots \\ \Delta\phi_N^*(t) \end{bmatrix} \quad (23)$$

is T^* -periodic. Functions of the form (22) are termed *D-periodic* or *derivo-periodic* with period T^* [43]. $\{\Delta\phi_i^*(t)\}$ represent short-term phase changes within each cycle that do not affect the long-term frequency of the oscillator.

The previous considerations motivate:

Assumption 3.2

$\vec{\phi}^*(t)$, the phase of the CPS during externally unperturbed lock, is T^* -D-periodic.

3.1.4. *Arbitrary time shifts of $\vec{\phi}^*(t)$ are also solutions of the CPS.*

Lemma 3.1

The phase during externally unperturbed lock, $\vec{\phi}^*(t)$, is not unique. Indeed, for any arbitrary time-shift τ ,

$$\vec{\phi}^*(t - \tau) \quad (24)$$

solves (16).

Proof

This follows directly from substituting (24) in the autonomous system (16) and using the facts that (1) $\vec{g}_\phi(\cdot)$ in (13) is cylindrical with period 1 and (2) $\vec{\phi}^*(t)$ is T^* -D-periodic (Assumption 3.2). \square

3.2. Periodic time-varying linearization of the CPS

3.2.1. *Linearization under small-deviation assumption.* If the external inputs $\{\vec{a}_i(t)\}$ are small, then $\vec{b}_\phi(\vec{\phi}, t)$ is small and (11) constitutes a small perturbation of (16). We express $\vec{\phi}(t)$, the solution of (11), as a deviation from $\vec{\phi}^*(t)$, the solution of (16):

$$\vec{\phi}(t) = \vec{\phi}^*(t) + \overrightarrow{\delta\phi}(t). \quad (25)$$

We term $\overrightarrow{\delta\phi}(t)$ the *orbital deviation*. Using (25), we now attempt to solve (11) via linearization.

Assumption 3.3

$\overrightarrow{\delta\phi}(t)$ remains small for all t , provided the external input $\vec{b}_\phi(\cdot, \cdot)$ is small enough for all t .^{††}

Applying Assumption 3.3, we start the process of linearizing (11):

$$\frac{d}{dt}\vec{\phi}^*(t) + \frac{d}{dt}\overrightarrow{\delta\phi}(t) \simeq \vec{g}_\phi(\vec{\phi}^*(t)) + \frac{\partial \vec{g}_\phi}{\partial \vec{\phi}}(\vec{\phi}^*(t))\overrightarrow{\delta\phi}(t) + \vec{b}_\phi(\vec{\phi}(t), t). \quad (26)$$

^{||} $\Delta\phi_i^*(t)$ can in fact itself satisfy (19) with arbitrary n , but $n \neq 0$ would make the long-term frequency of $x_{p,i}(\phi_i(t))$ different from f^* , violating Assumption 3.1.

^{**}We use the notation, borrowed from MATLAB, that the sum of a scalar and a vector means that the scalar is added to each element of the vector.

^{††}That is, $\|\overrightarrow{\delta\phi}(t)\| < M \|\vec{b}_\phi(\cdot, \cdot)\|$ for some finite constant $M > 0$.

Using (16), we obtain

$$\begin{aligned} \frac{d}{dt} \vec{\delta\phi}(t) &\simeq \frac{\partial \vec{g}_\phi}{\partial \vec{\phi}} \left(\vec{\phi}^*(t) \right) \vec{\delta\phi}(t) + \vec{b}_\phi \left(\vec{\phi}(t), t \right) \\ &\simeq \frac{\partial \vec{g}_\phi}{\partial \vec{\phi}} \left(\vec{\phi}^*(t) \right) \vec{\delta\phi}(t) + \vec{b}_\phi \left(\vec{\phi}^*(t), t \right) + \frac{\partial \vec{b}_\phi}{\partial \vec{\phi}} \left(\vec{\phi}^*(t), t \right) \vec{\delta\phi}(t) \\ &= \left(\frac{\partial \vec{g}_\phi}{\partial \vec{\phi}} \left(\vec{\phi}^*(t) \right) + \frac{\partial \vec{b}_\phi}{\partial \vec{\phi}} \left(\vec{\phi}^*(t), t \right) \right) \vec{\delta\phi}(t) + \vec{b}_\phi \left(\vec{\phi}^*(t), t \right). \end{aligned} \quad (27)$$

From the definition of $\vec{b}_\phi(\cdot, \cdot)$ (14), observe that $\frac{\partial \vec{b}_\phi}{\partial \vec{\phi}} \left(\vec{\phi}^*(t), t \right)$ is a diagonal matrix with entries^{‡‡}

$$f_i \vec{p}_i'^T \left(\phi_i^*(t) \right) \vec{a}_i(t),$$

that is, it is directly proportional to the external inputs $\{\vec{a}_i(t)\}$, which are small by assumption. Therefore, the product term $\frac{\partial \vec{b}_\phi}{\partial \vec{\phi}} \left(\vec{\phi}^*(t), t \right) \vec{\delta\phi}(t)$ in (27) is of second order and can be dropped from the linearization. Applying this observation and denoting

$$J_\phi^*(t) \triangleq \frac{\partial \vec{g}_\phi}{\partial \vec{\phi}} \left(\vec{\phi}^*(t) \right), \text{ and} \quad (28)$$

$$\vec{b}_{\text{ext}}(t) \triangleq \vec{b}_\phi \left(\vec{\phi}^*(t), t \right), \quad (29)$$

(27) becomes

$$\boxed{\frac{d}{dt} \vec{\delta\phi}(t) \simeq J_\phi^*(t) \vec{\delta\phi}(t) + \vec{b}_{\text{ext}}(t)}. \quad (30)$$

(30) is the linearization of the CPS (11) around its externally unperturbed solution $\vec{\phi}^*(t)$.

3.2.2. T^* -periodicity of $J_\phi^*(t)$. From (13), we can obtain expressions for the entries of $J_\phi^*(t)$. The diagonal entries of J_ϕ^* are

$$J_{\phi_{i,j}}^*(t) = f_i \vec{p}_i'^T \left(\phi_i^*(t) \right) \sum_{\substack{j \neq i \\ j=1}}^N \vec{b}_{ij} \left(\phi_j^*(t) \right), \quad (31)$$

while the off-diagonal entries are

$$J_{\phi_{i,j}}^*(t) = f_i \vec{p}_i'^T \left(\phi_i^*(t) \right) \vec{b}_{ij}' \left(\phi_j^*(t) \right). \quad (32)$$

Because of the one-periodicity of $\vec{p}_i(\cdot)$ and $\vec{b}_{ij}(\cdot)$, and the T^* -D-periodicity of $\phi_i^*(t)$, each entry of J_ϕ^* is T^* -periodic; hence, the entire matrix function $J_\phi^*(t)$ is T^* -periodic. The linearized CPS (30) is therefore periodically time varying, that is, it is a *linear periodically time varying (LPTV)* system.

^{‡‡}For any function $f(\cdot)$, $f'(\cdot)$ denotes the derivative wrt the argument.

3.3. T^* -periodic homogeneous solution of the linearized CPS

Lemma 3.2

The homogeneous part of the linearized CPS (30), that is,

$$\frac{d}{dt}\vec{\delta\phi}(t) = J_{\phi}^*(t) \vec{\delta\phi}(t), \quad (33)$$

has the T^* -periodic solution

$$\vec{\delta\phi}^*(t) \triangleq \frac{d}{dt}\vec{\phi}^*(t). \quad (34)$$

Proof

This follows immediately from differentiating (16). Note that T^* -D-periodicity of $\vec{\phi}^*(t)$ immediately implies that $\vec{\delta\phi}^*(t)$ in (34) is T^* -periodic, because

$$\vec{\delta\phi}^*(t) = f^* + \frac{d}{dt}\vec{\Delta\phi}^*(t), \quad (35)$$

with the latter term T^* -periodic. \square

3.4. Floquet-theoretic solution of the linearized CPS

Floquet theory [43] provides an analytical form^{§§} for the solution of (30):

$$\vec{\delta\phi}(t) = U(t)D(t-t_0)V^T(t_0)\vec{\delta\phi}_0 + U(t)\int_{t_0}^t D(t-\tau)V^T(\tau)\vec{b}_{\text{ext}}(\tau)d\tau. \quad (36)$$

$U(t)$ and $V^T(t)$ are T^* -periodic matrix functions, of size $N \times N$, that satisfy

$$U(t)V^T(t) = V^T(t)U(t) = I_{N \times N}. \quad (37)$$

Equation (37) implies that the columns of U and V are bi-orthogonal, that is,

$$\vec{v}_i^T(t)\vec{u}_j(t) = \delta_{ij}, \quad i, j = 1, \dots, N. \quad (38)$$

Equation (37) can be written more explicitly, showing \vec{v}_i and \vec{u}_j , as

$$\begin{pmatrix} \dots \vec{v}_1^T(t) \dots \\ \vdots \\ \dots \vec{v}_N^T(t) \dots \end{pmatrix} \begin{pmatrix} \vdots & & \vdots \\ \vec{u}_1(t) & \dots & \vec{u}_N(t) \\ \vdots & & \vdots \end{pmatrix} \equiv \begin{pmatrix} 1 & & \\ & \ddots & \\ & & 1 \end{pmatrix}. \quad (39)$$

Note that, in particular,

$$\vec{v}_1^T(t)\vec{u}_1(t) \equiv 1, \forall t, \quad (40)$$

a relation we will rely on later.

^{§§}Equation (36) holds for the case where the Floquet multipliers (41) are distinct, but subject to Assumption 3.4; all subsequent results in this section remain valid for the case of repeated Floquet multipliers.

$D(\cdot)$ in (36) is a *diagonal* matrix of the form

$$D(t) = \begin{pmatrix} e^{\mu_1 t} & & \\ & \ddots & \\ & & e^{\mu_N t} \end{pmatrix}, \quad (41)$$

where $\{\mu_i\}$ are termed *Floquet* or *characteristic exponents*, and

$$\rho_i \triangleq e^{\mu_i T^*}, \quad i = 1, \dots, N, \quad (42)$$

are known as *Floquet* or *characteristic multipliers*. Note that $D(t)$ is not periodic.

Equation (36) can be rewritten using $\vec{v}_i(\cdot)$ and $\vec{u}_i(\cdot)$ as

$$\vec{\delta\phi}(t) = \sum_{i=1}^N \vec{u}_i(t) \underbrace{e^{\mu_i(t-t_0)} \vec{v}_i^T(t_0) \vec{\delta\phi}_0}_{\text{scalar}} + \sum_{i=1}^N \vec{u}_i(t) \underbrace{\int_{t_0}^t e^{\mu_i(t-\tau)} \vec{v}_i^T(\tau) \vec{b}_{\text{ext}}(\tau) d\tau}_{\text{scalar}}. \quad (43)$$

3.5. Conditions on Floquet multipliers; stability and isolation of $\vec{\phi}^*(t)$

Lemma 3.1 suggests that the stability of the CPS (11) around its locked solution (15) in the absence of external inputs is of an orbital nature [43, Definition 5.1.1] and not, for example, of a Lyapunov one [43, Definition 1.4.1].

Lemma 3.3

At least one of the Floquet multipliers $\{\rho_i\}$ (42) is 1 (equivalently, at least one of the Floquet exponent $\{\mu_i\}$ is 0).

Proof

This follows from the existence of the T^* -periodic homogeneous solution of the linearized CPS (35), established in Lemma 3.2, and [43, Corollary 2.2.3]. \square

Lemma 3.4

$|\rho_i| \leq 1, \forall i$ (equivalently, $\Re(\mu_i) \leq 0$).

Proof

This follows from Assumption 3.1 (i.e. that the externally unperturbed oscillator system is mutually injection locked in a *stable* orbit) and [43, Theorem 5.1.3]. \square

We now make an additional technical assumption regarding the Floquet multipliers:

Assumption 3.4

Only one Floquet multiplier (ρ_1 , without loss of generality) is 1 (equivalently, w.l.o.g, $\mu_1 = 0$).

Note that Assumption 3.4 strengthens Lemma 3.3. There are several factors that motivate this assumption:

- (1) Assumption 3.4, together with Lemma 3.4, constitutes *sufficient* conditions for the Andronov–Witt theorem [43, Theorems 5.3.8 and 5.1.2] to hold. The Andronov–Witt theorem guarantees that the CPS (11) is *asymptotically orbitally stable (a.o.s)* [43, Definition 5.1.2] with the *asymptotic phase property (a.o.p)* [43, Definition 5.1.3]. These properties are central to the intuitive concept of stable lock, assumed in Assumption 3.1 and typically valid in most applications.
- (2) Assumption 3.4 also constitutes a sufficient condition for the orbit $\vec{\phi}^*(t)$ (15) to be *isolated*, that is, not embedded in a continuum of orbits with continuously varying periods [43, Theorems 5.3.9 and 5.2.3]. Isolation is also central to the intuitive notion of stable lock.

- (3) Although Assumption 3.4 is not a *necessary* condition for asymptotic orbital stability with the asymptotic phase property, or for isolation, oscillators that do not satisfy the assumption while still being a.o.s + a.o.p tend to be ‘unnatural’. For example, Farkas [43, Example 5.2.2] features an orbit that is a.o.s + a.o.p but has three repeated Floquet multipliers that equal 1; however, this orbit is not periodic.

Thus, in most practical situations, Assumption 3.4 is essentially equivalent to the oscillator group’s being ‘stably locked’.

3.6. Assumption 3.3 (deviations are small) is invalid

Lemma 3.5

Assumption 3.3 is invalid.

Proof

Using Assumption 3.4, the second summation term of (43), which captures the linearized system’s response to external perturbations $\vec{b}_{\text{ext}}(t)$, can be written as

$$\vec{u}_1(t) \int_{t_0}^t \overbrace{\vec{v}_1^T(\tau) \vec{b}_{\text{ext}}(\tau)}^{\text{scalar } c_1(t)} d\tau + \sum_{i=2}^N \vec{u}_i(t) \int_{t_0}^t \underbrace{e^{\mu_i(t-\tau)} \vec{v}_i^T(\tau) \vec{b}_{\text{ext}}(\tau)}_{\text{scalar } c_i(t)} d\tau. \quad (44)$$

The first term is of the form $c_1(t)\vec{u}_1(t)$, where $c_1(t)$ is the scalar

$$c_1(t) = \int_{t_0}^t \vec{v}_1^T(\tau) \vec{b}_{\text{ext}}(\tau) d\tau. \quad (45)$$

Because $\vec{v}_1(\tau)$ is periodic, there exist many possibilities for small $\vec{b}_{\text{ext}}(t)$ that make $c_1(t)$ increase indefinitely and without bound as t increases. For example, if $\vec{b}_{\text{ext}}(t) = \epsilon \vec{u}_1(t)$, with $\epsilon \neq 0$ being any constant, then, from (40), $c_1(t) = (t - t_0)\epsilon$; that is, $c_1(t)$ increases without bound. The remaining terms in (44) are bounded because $\Re(\mu_i) < 0$, $\forall i > 1$, hence cannot cancel the unbounded increase of the first term.

In other words, Assumption 3.3, upon which the linearized system (30), its solution (36), and indeed, the expression for the unbounded term $c_1(t)$ in (45) all depend, is violated. Thus, we have arrived at a contradiction, implying that the original premise Assumption 3.3 must be invalid (subject to the other assumptions’ validity). \square

That deviations can grow to be large even when external inputs remain small is a manifestation of the inherently marginal nature of orbital stability, that is, that $\mu_1 = 0$.

3.7. Time-shifted perturbed response assumption

Lemma 3.6

Without loss of generality,

$$\vec{u}_1(t) = \vec{\delta\phi}^*(t) = \frac{d}{dt} \vec{\phi}^*(t). \quad (46)$$

Proof

The first summation term in (43), that is,

$$\sum_{i=1}^N \vec{u}_i(t) \underbrace{e^{\mu_i(t-t_0)} \vec{v}_i^T(t_0) \vec{\delta\phi}_0}_{\text{scalar}}, \quad (47)$$

represents a general solution of (33). We already know that $\vec{\delta\phi}^*(t)$ (34) is a nontrivial *periodic* solution of (33). Using $\rho_1 = 1$ from Assumption 3.4, this periodic solution must equal the $i = 1$

term in (47), because (also from Assumption 3.4) the remaining terms for $i = 2, \dots, N$ are not periodic and indeed, decay to 0 as $t \rightarrow \infty$. Hence, we have

$$\vec{\delta\phi}^*(t) = k_2 \vec{u}_1(t) \underbrace{\vec{v}_1^T(t_0) \vec{\delta\phi}^*(t_0)}_{\text{scalar constant } k_1}. \quad (48)$$

where k_2 is an arbitrary scalar constant. Note that $k_1 \neq 0$; otherwise, (47) would be identically zero, hence would not match any nontrivial $\vec{\delta\phi}^*(t)$. Choosing $k_2 = \frac{1}{k_1}$ (without loss of generality, because $\vec{v}_1(t)$ can be scaled to satisfy (40)) results in (46). \square

Geometrically, $\frac{d}{dt}\vec{\phi}^*(t)$ is the tangent to the externally unperturbed orbit of the locked system in phase space; Lemma 3.6 thus justifies the terminology *tangent vector* for $\vec{u}_1(t)$.

Attempting to restore validity to the failed linearization procedure previously discussed, observe that using (46), the unbounded term in (45) can be written as

$$c_1(t)\vec{u}_1(t) = c_1(t)\frac{d}{dt}\vec{\phi}^*(t). \quad (49)$$

Observe also that if $c_1(t)$ were bounded and small, then

$$\vec{\phi}^*(t) + c_1(t)\frac{d}{dt}\vec{\phi}^*(t) \simeq \vec{\phi}^*(t + c_1(t)), \quad (50)$$

to the first order. This suggests that the unboundedly growing component of $\vec{\delta\phi}(t)$ in (43) may be the manifestation of a time-shift to the unperturbed solution $\vec{\phi}^*(t)$. A time shift along the orbit is also suggested by the definition of orbital stability [43, Definition 5.1.1] and by the physical intuition that autonomous oscillators, having no intrinsic ‘time reference’, can ‘slip in phase’; that is, they cannot correct errors in phase. Accordingly, we modify the assumed form of the perturbed solution (25) to

Assumption 3.5

$$\vec{\phi}(t) = \vec{\phi}^*(t + \alpha_g(t)) + \vec{\delta\phi}(t), \quad (51)$$

where $\vec{\delta\phi}(t)$ remains small for all time (i.e. $\|\vec{\delta\phi}(t)\| < M \|\vec{b}_{\text{ext}}(t)\|$ for some finite $M > 0$).

$\alpha_g(t)$ is a (yet-to-be-determined) time shift that can depend on the input perturbation $\vec{b}_{\text{ext}}(t)$ and can grow unboundedly with time. Importantly, we have retained Assumption 3.3, that is, that $\vec{\delta\phi}(t)$ in (51) remains bounded and small for all time.

We shall prove that unlike (25), the time-shifted deviation form (51) will allow $\vec{\delta\phi}(t)$ to remain bounded and small, providing the time-shift $\alpha_g(t)$ is chosen appropriately.

3.8. Base for time-shifted linearization

In Section 3.2, the CPS was linearized around the unperturbed orbit $\vec{\phi}^*(t)$. The process of linearization relied on the fact that $\vec{\phi}^*(t)$ satisfied (16). We would like to find a replacement for (16) that is satisfied by

$$\vec{\phi}(t) = \vec{\phi}^*(t + \alpha_g(t)) \quad (52)$$

instead.

Lemma 3.7

Given any scalar, differentiable function $\alpha_g(t)$, the CPS (11) is solved exactly by (52) for perturbations of the form

$$\vec{b}_\phi(\vec{\phi}(t), t) \triangleq K(t)\vec{u}_1(t + \alpha_g(t)), \quad (53)$$

where $K(t) \equiv \frac{d}{dt}\alpha_g(t)$.

Proof

Denoting ‘shifted time’ to be

$$t^\dagger \triangleq t + \alpha_g(t), \quad (54)$$

substituting (52) and (53) into (11) and simplifying using (16) and (46), we obtain

$$\begin{aligned} (1 + \dot{\alpha}_g(t)) \frac{d}{dt^\dagger} \vec{\phi}^*(t^\dagger) &= \vec{g}_\phi(\vec{\phi}^*(t^\dagger)) + K(t)\vec{u}_1(t^\dagger) \\ \Rightarrow \dot{\alpha}_g(t) \frac{d}{dt^\dagger} \vec{\phi}^*(t^\dagger) &= K(t)\vec{u}_1(t^\dagger) \\ \Rightarrow \dot{\alpha}_g(t)\vec{u}_1(t^\dagger) &= K(t)\vec{u}_1(t^\dagger) \\ \Rightarrow \dot{\alpha}_g(t)\vec{u}_1(t + \alpha_g(t)) &= K(t)\vec{u}_1(t + \alpha_g(t)). \end{aligned} \quad (55)$$

Equation (55) is always satisfied if $\alpha_g(t)$ and $K(t)$ are related by

$$\dot{\alpha}_g(t) = K(t). \quad (56)$$

□

3.9. Time-shifted linearization

We proceed to linearize the CPS (11) around solutions of the form (52). To this end, we split the external input $\vec{b}_\phi(\vec{\phi}, t)$ (14) into two parts:

$$\vec{b}_\phi(\vec{\phi}, t) = \vec{b}_{\phi_1}(t) + \vec{b}_{\phi_2}(\vec{\phi}, t), \quad (57)$$

with the intent that if only the first component $\vec{b}_{\phi_1}(t)$ is retained, then (52) should solve the CPS (11) *exactly*, that is,

$$\frac{d}{dt} \vec{\phi}^*(t + \alpha_g(t)) = \vec{g}_\phi(\vec{\phi}^*(t + \alpha_g(t))) + \vec{b}_{\phi_1}(t). \quad (58)$$

Motivated by Lemma 3.7, we explore perturbations of the form (53) along the tangent vector, that is, of the form

$$\vec{b}_{\phi_1}(t) = K(t)\vec{u}_1(t + \alpha_g(t)). \quad (59)$$

Given any small external perturbation $\vec{b}_\phi(\vec{\phi}(t), t)$ (14), our goal is to find such an $\alpha_g(t)$ (and, using Lemma 3.7, its derivative $K(t)$) that $\vec{b}_{\phi_2}(\cdot, \cdot)$ in (57) and the orbital deviation $\vec{\delta}\vec{\phi}(t)$ in (51), both remain small.

The flow of the time-shifted linearization procedure is as follows:

- (1) Start by assuming *any* scalar function $K(t)$.
- (2) Define $\alpha_g(t)$ using (56), that is, $\frac{d}{dt}\alpha_g(t) = K(t)$.

- (3) Define $\vec{b}_{\phi_1}(t)$ using (59).
- (4) Incorporate the split-up form (57) of the external input perturbation in the CPS (11).
- (5) Assuming a solution of the form (51) in Assumption 3.5, linearize (11) using (58) as the base case.
- (6) Using the solution of the previous linearization, obtain a constraint on $\alpha_g(t)$ (equivalently, on $K(t)$) under which Assumption 3.5 holds with $\vec{\delta\phi}(t)$ bounded and small for all time. The equation specifying this constraint will turn out to be of central importance, in that it governs the phase/timing responses of the injection-locked system of oscillators to external perturbations.
- (7) When $\alpha_g(t)$ (equivalently, its derivative $K(t)$) is chosen to satisfy the aforementioned constraint, show that the phase deviation $\vec{\delta\phi}(t)$ in (51) always remains small, thus validating Assumption 3.5 and the entire time-shifted linearization procedure.

Starting from Step 4, write the CPS (11) as

$$\frac{d}{dt}\vec{\phi}(t) = \vec{g}_{\phi}(\vec{\phi}(t)) + \vec{b}_{\phi_1}(t) + \vec{b}_{\phi_2}(\vec{\phi}(t), t). \quad (60)$$

Incorporating (51), (56) and (59) in (60), we obtain

$$\begin{aligned} \frac{d}{dt} [\vec{\phi}^*(t + \alpha_g(t)) + \vec{\delta\phi}(t)] &= \vec{g}_{\phi}(\vec{\phi}^*(t + \alpha_g(t)) + \vec{\delta\phi}(t)) \\ &\quad + K(t)\vec{u}_1(t + \alpha_g(t)) + \vec{b}_{\phi_2}(\vec{\phi}^*(t + \alpha_g(t)) + \vec{\delta\phi}(t), t). \end{aligned} \quad (61)$$

Linearizing $\vec{g}_{\phi}(\cdot)$ in (61), we obtain

$$\begin{aligned} \frac{d}{dt}\vec{\phi}^*(t + \alpha_g(t)) + \frac{d}{dt}\vec{\delta\phi}(t) &= \vec{g}_{\phi}(\vec{\phi}^*(t + \alpha_g(t))) \\ &\quad + J_{\phi}^*(t + \alpha_g(t))\vec{\delta\phi}(t) + K(t)\vec{u}_1(t + \alpha_g(t)) \\ &\quad + \vec{b}_{\phi_2}(\vec{\phi}^*(t + \alpha_g(t)) + \vec{\delta\phi}(t), t). \end{aligned} \quad (62)$$

Applying the base for time-shifted linearization (58) and our proposed form (59) for $\vec{b}_{\phi_1}(t)$, (62) can be simplified to

$$\frac{d}{dt}\vec{\delta\phi}(t) = J_{\phi}^*(t + \alpha_g(t))\vec{\delta\phi}(t) + \vec{b}_{\phi_2}(\vec{\phi}^*(t + \alpha_g(t)) + \vec{\delta\phi}(t), t). \quad (63)$$

Observe that from definition (57), (59),

$$\vec{b}_{\phi_2}(\vec{\phi}^*(t + \alpha_g(t)) + \vec{\delta\phi}(t), t) = \vec{b}_{\phi}(\vec{\phi}^*(t + \alpha_g(t)) + \vec{\delta\phi}(t), t) - K(t)\vec{u}_1(t + \alpha_g(t)), \quad (64)$$

hence, (63) can be written as

$$\begin{aligned} \frac{d}{dt}\vec{\delta\phi}(t) &= J_{\phi}^*(t + \alpha_g(t))\vec{\delta\phi}(t) - K(t)\vec{u}_1(t + \alpha_g(t)) \\ &\quad + \vec{b}_{\phi}(\vec{\phi}^*(t + \alpha_g(t)) + \vec{\delta\phi}(t), t). \end{aligned} \quad (65)$$

Using the same reasoning as for (27) in Section 3.2.1, $\vec{\delta\phi}(t)$ in the last term of (65) can be dropped because it contributes only a second-order term to the linearization. Hence, (65) becomes

$$\begin{aligned}\frac{d}{dt}\vec{\delta\phi}(t) &= J_{\phi}^*(t + \alpha_g(t))\vec{\delta\phi}(t) - K(t)\vec{u}_1(t + \alpha_g(t)) \\ &\quad + \vec{b}_{\phi}(\vec{\phi}^*(t + \alpha_g(t)), t) \\ &= J_{\phi}^*(t^{\dagger})\vec{\delta\phi}(t) + \vec{b}_{\phi}(\vec{\phi}^*(t^{\dagger}), t) - K(t)\vec{u}_1(t^{\dagger}) \\ &= J_{\phi}^*(t^{\dagger})\vec{\delta\phi}(t) + \vec{b}_{\phi_2}(\vec{\phi}^*(t^{\dagger}), t),\end{aligned}\tag{66}$$

where we have used the notation t^{\dagger} , defined in (54), for shifted time.

3.10. Recasting time-shifted linearization in LPTV form

We would now like to obtain an analytical solution of (66) and use it to validate that $\vec{\delta\phi}(t)$ remains small for all time. However, two differences between (30) and (66) make this more involved than for (30) in Section 3.4:

- (1) The input to (66) is $\vec{b}_{\phi_2}(\cdot, \cdot)$, not $\vec{b}_{\phi}(\cdot, \cdot)$ as in (30). Whereas the latter is known small (due to the assumption of small external perturbations $\{a_i(t)\}$ in (14)), there is no guarantee that $\vec{b}_{\phi_2}(\cdot, \cdot)$ is also small. Ensuring that $\vec{b}_{\phi_2}(\cdot, \cdot)$ is small is important: even if the input to (66) cannot be guaranteed small, it is unreasonable to expect that its solution will remain small for all time.
- (2) Unlike (30), which is LPTV, (66) is *not* LPTV because although $J_{\phi}^*(t)$ is T^* -periodic, $J_{\phi}^*(t + \alpha_g(t))$ is not, except for special choices such as $\alpha_g(t) \equiv 0$. We are interested in a solution of (66) that is valid for any $\alpha_g(t)$ (equivalently, any $K(t)$), if possible. Because (66) is not LPTV, the Floquet expressions in Section 3.4 do not apply directly.

Both issues can be addressed by restricting $\dot{\alpha}_g(t) \equiv K(t)$ to be small. We state this as an assumption for the moment^{¶¶}:

Assumption 3.6

$$K(t) \triangleq \dot{\alpha}_g(t)\tag{67}$$

is small and bounded with respect to $\vec{b}_{\phi}(\cdot, \cdot)$ (14) for all time. In particular, $|K(t)| \ll 1$.

The first consequence of Assumption 3.6 is that it becomes possible to guarantee that $\vec{b}_{\phi_2}(\cdot, \cdot)$, the input to the time-shifted linearization (66), is small:

Lemma 3.8
 $\vec{b}_{\phi_2}(\vec{\phi}^*(t^{\dagger}), t)$ is small for all t^{\dagger}, t .

Proof

From definition (57),

$$\vec{b}_{\phi_2}(\vec{\phi}^*(t^{\dagger}), t) = \vec{b}_{\phi}(\vec{\phi}^*(t^{\dagger}), t) - K(t)\vec{u}_1(t^{\dagger}).\tag{68}$$

The first term is small from our underlying assumption of small external perturbations. The tangent vector $\vec{u}_1(t)$ is a periodic, bounded quantity; hence, under Assumption 3.6, the second term is also small. \square

^{¶¶}We will establish later that this assumption is in fact a consequence of the external inputs $\vec{b}_{\phi}(\cdot, \cdot)$ being small.

Another important consequence of Assumption 3.6 is the following:

Lemma 3.9

The mapping (54)

$$t \mapsto t^\dagger, \text{ that is, } t^\dagger(t) \triangleq t + \alpha_g(t)$$

is invertible.

Proof

It suffices to show that the mapping is a monotonically increasing one, that is, its derivative is always positive. We have

$$\frac{d}{dt}t^\dagger(t) = 1 + \dot{\alpha}_g(t) = 1 + K(t).$$

From Assumption 3.6, $|K(t)| < 1$; hence, $\frac{d}{dt}t^\dagger(t) > 0$, that is, $t^\dagger(t)$ is monotonically increasing. \square

We now make the following definitions:

$$\vec{\delta\phi}^\dagger(t^\dagger) \triangleq \vec{\delta\phi}(t), \quad (69)$$

$$\vec{b}_{\phi_2}^\dagger(a, t^\dagger) \triangleq \vec{b}_{\phi_2}(a, t), \text{ and} \quad (70)$$

$$\vec{b}_\phi^\dagger(a, t^\dagger) \triangleq \vec{b}_\phi(a, t). \quad (71)$$

The significance of the invertibility of shifted time t^\dagger , as established by Lemma 3.9, lies in that the previous definitions become possible: given any t^\dagger , a unique t is available for use in the right hand sides of the previous definitions.

Using the previous definitions, (66) can be expressed using t^\dagger as

$$(1 + \dot{\alpha}_g(t)) \frac{d}{dt^\dagger} \vec{\delta\phi}^\dagger(t^\dagger) = J_\phi^*(t^\dagger) \vec{\delta\phi}^\dagger(t^\dagger) + \vec{b}_{\phi_2}^\dagger(\vec{\phi}^*(t^\dagger), t^\dagger). \quad (72)$$

We now make a technical assumption for the moment, the validity of which will be demonstrated later:

Assumption 3.7

$$\left\| \frac{d}{dt} \vec{\delta\phi}(t) \right\| < M \left\| \vec{\delta\phi}(t) \right\| \text{ for some } 0 < M < \infty.$$

Assumption 3.7 implies that the magnitude of $\frac{d}{dt} \vec{\delta\phi}(t)$ is within a constant factor of the magnitude of $\vec{\delta\phi}(t)$, that is, the two are of the same order of magnitude. Intuitively, it implies that $\vec{\delta\phi}(t)$ has a bounded rate of change. It follows that $\vec{\delta\phi}^\dagger(t^\dagger)$ also has a bounded rate of change:

Lemma 3.10

$$\left\| \frac{d}{dt^\dagger} \vec{\delta\phi}^\dagger(t^\dagger) \right\| < M_2 \left\| \vec{\delta\phi}^\dagger(t^\dagger) \right\| \text{ for some } 0 < M_2 < \infty.$$

Proof

Using (69), (54) and (56), we have

$$\frac{d}{dt^\dagger} \vec{\delta\phi}^\dagger(t^\dagger) = \frac{d}{dt^\dagger} \vec{\delta\phi}(t) = \frac{1}{1 + K(t)} \frac{d}{dt} \vec{\delta\phi}(t).$$

Because $|K(t)| \ll 1$ from Assumption 3.6, we have $\left\| \frac{d}{dt^\dagger} \vec{\delta\phi}^\dagger(t^\dagger) \right\| < m \left\| \frac{d}{dt} \vec{\delta\phi}(t) \right\|$ for some $m < \infty$. Using Assumption 3.7, the result follows. \square

From Lemma 3.10, it is apparent that the term $\dot{\alpha}_g \frac{d}{dt^\dagger} \vec{\delta\phi}^\dagger(t^\dagger)$ in (72) is of second order, hence can be dropped from the linearization. As a result, (72) becomes

$$\frac{d}{dt^\dagger} \vec{\delta\phi}^\dagger(t^\dagger) = J_\phi^*(t^\dagger) \vec{\delta\phi}^\dagger(t^\dagger) + \vec{b}_{\phi_2}^\dagger(\vec{\phi}^*(t^\dagger), t^\dagger). \quad (73)$$

Note that (73) is an LPTV system, because $J_\phi^*(t^\dagger)$ is periodic in t^\dagger with period T^* .

3.11. Floquet solution of time-shifted LPTV system

Because (73) is LPTV, the Floquet expressions in Section 3.4 apply, with t and $\vec{\delta\phi}(t)$ replaced by t^\dagger and $\vec{\delta\phi}^\dagger(t^\dagger)$, respectively, and $\vec{b}_{\text{ext}}(t)$ replaced by $\vec{b}_{\phi_2}^\dagger(\vec{\phi}^*(t^\dagger), t^\dagger)$. Equation (43) becomes

$$\vec{\delta\phi}^\dagger(t^\dagger) = \sum_{i=1}^N \vec{u}_i(t^\dagger) \underbrace{e^{\mu_i(t^\dagger - t_0^\dagger)} \vec{v}_i^T(t_0^\dagger)}_{\text{scalar}} \vec{\delta\phi}^\dagger(t_0^\dagger) + \sum_{i=1}^N \vec{u}_i(t^\dagger) \underbrace{\int_{t_0^\dagger}^{t^\dagger} e^{\mu_i(t^\dagger - \tau)} \vec{v}_i^T(\tau) \vec{b}_{\phi_2}^\dagger(\vec{\phi}^*(\tau), \tau) d\tau}_{\text{scalar}}, \quad (74)$$

while the term $c_1(t)$ in (45), which causes unbounded growth and resulting breakdown of linearization, becomes

$$c_1^\dagger(t^\dagger) \triangleq \int_{t_0^\dagger}^{t^\dagger} \vec{v}_1^T(\tau) \vec{b}_{\phi_2}^\dagger(\vec{\phi}^*(\tau), \tau) d\tau. \quad (75)$$

3.12. Choosing $\alpha_g(t)$ to circumvent breakdown of linearization

To avoid unbounded growth of $\vec{\delta\phi}^\dagger(t^\dagger)$, which would invalidate the present time-shifted linearization procedure in the same manner as Section 3.6 and Lemma 3.5 previously, it is imperative that $c_1^\dagger(t^\dagger)$ in (75) remains small and bounded (with respect to $\vec{b}_{\phi_2}^\dagger(\cdot, \cdot)$). This can be achieved by the simple expedient of requiring that the integrand in (75) vanishes, that is,

$$\vec{v}_1^T(\tau) \vec{b}_{\phi_2}^\dagger(\vec{\phi}^*(\tau), \tau) \equiv 0, \forall \tau. \quad (76)$$

Substituting t^\dagger for τ in (76), and applying (70), (68), (40), (67) and (54), we obtain

$$\begin{aligned} 0 &= \vec{v}_1^T(\tau) \vec{b}_{\phi_2}^\dagger(\vec{\phi}^*(\tau), \tau) \\ \Rightarrow 0 &= \vec{v}_1^T(t^\dagger) \vec{b}_{\phi_2}^\dagger(\vec{\phi}^*(t^\dagger), t^\dagger) \\ \Rightarrow 0 &= \vec{v}_1^T(t^\dagger) [\vec{b}_\phi(\phi^*(t^\dagger), t) - K(t) \vec{u}_1(t^\dagger)] \\ \Rightarrow K(t) \vec{v}_1^T(t^\dagger) \vec{u}_1(t^\dagger) &= \vec{v}_1^T(t^\dagger) \vec{b}_\phi(\phi^*(t^\dagger), t) \\ \Rightarrow K(t) &= \vec{v}_1^T(t^\dagger) \vec{b}_\phi(\phi^*(t^\dagger), t) \\ \Rightarrow \dot{\alpha}_g(t) &= \vec{v}_1^T(t^\dagger) \vec{b}_\phi(\phi^*(t^\dagger), t) \\ \Rightarrow \boxed{\frac{d}{dt} \alpha_g(t) = \vec{v}_1^T(t + \alpha_g(t)) \vec{b}_\phi(\vec{\phi}^*(t + \alpha_g(t)), t)}. \end{aligned} \quad (77)$$

From the considerations of Section 3.9 to (77), we are able to prove the following Theorem:

Theorem 1

Given a system of N coupled oscillators modelled in the phase domain by the CPS equations (11) and mutually injection locked, satisfying Assumption 3.1 and Assumption 3.4. If the external

perturbations to the system $\{a_i(t)\}$ (10) (equivalently, $\vec{b}_\phi(\cdot, \cdot)$ in (11) are small, and if $\alpha_g(t)$ is chosen to satisfy (77), that is,

$$\frac{d}{dt}\alpha_g(t) = \vec{v}_1^T(t + \alpha_g(t))\vec{b}_\phi(\vec{\phi}^*(t + \alpha_g(t)), t),$$

then the solution of the CPS can be expressed as in (51), that is, as

$$\vec{\phi}(t) = \vec{\phi}^*(t + \alpha_g(t)) + \vec{\delta\phi}(t),$$

where $\vec{\phi}^*(t)$ is the periodic, synchronized solution of the externally unperturbed system of oscillators. $\vec{\delta\phi}(t)$, the deviations from the orbit of the externally unperturbed system, remain small and bounded for all t (with respect to the external perturbations $\{a_i(t)\}$).

Proof

Subject to Assumption 3.5 and Assumption 3.6, Lemma 3.8 establishes that $\vec{b}_{\phi_2}(\vec{\phi}^*(t^\dagger), t)$ is small; applying (70) shows that $\vec{b}_{\phi_2}^\dagger(\cdot, \cdot)$, which appears in (74), is also small.

Choosing $\alpha_g(t)$ to satisfy (77) ensures that $c_1^\dagger(t^\dagger)$ (75) vanishes, as demonstrated previously. As a result, the $i = 1$ terms in (74) (which correspond to Floquet multiplier $\rho_1 = 1$ or equivalently, Floquet exponent $\mu_1 = 1$) remain bounded and small. From Assumption 3.4 and Lemma 3.4, the remaining Floquet exponents μ_2, \dots, μ_N all have strictly negative real parts. With $\vec{b}_{\phi_2}^\dagger(\cdot, \cdot)$ small as noted previously, this implies that the terms corresponding to $i = 2, \dots, N$ in (74) also remain bounded and small for all t . As a result, $\vec{\delta\phi}^\dagger(t^\dagger)$ remains bounded and small for all t . Applying (69), $\vec{\delta\phi}(t)$ also remains small and bounded for all time. This immediately validates Assumption 3.5. That $\vec{b}_\phi(\cdot, \cdot)$ is small (by assumption) and (77) holds also validates Assumption 3.6.

Differentiating (74) and proceeding in a similar manner, Assumption 3.7 can also be shown to be valid. \square

4. ILLUSTRATION, RESULTS AND VALIDATION

In this section, we demonstrate and validate the theory of Section 3 using homogeneous, as well as, heterogeneous networks of mechanical pendulum clocks, electronic ring oscillators based on CMOS architecture, and oscillatory neurons based on the FitzHugh–Nagumo model. While doing so, we also illustrate the computational efficiency and accuracy of the different ways in which we can abstract network models. We compare the network models obtained (and the locked waveforms predicted) by these different abstraction procedures. In Section 4.4, we work out in detail the computational complexity of the different abstraction procedures discussed, and thus derive the computational advantage gained by one procedure over the other. All computations and simulations were performed using MATLABTM on a single processor.

Figure 3 shows the general topology of the rectangular grid-type coupling that we will be using for all our examples. The double headed arrows signify two-way coupling between the neighbouring oscillators. We focus on networks of size 16×16 here.

Figure 4 depicts different ways of obtaining a reduced order model of the network (including obtaining different sized reduced order models). Each point (x, y) on this 16×16 grid corresponds to a $x \times y$ -sized network model. As we can see, even for obtaining a particular sized network model, there are multiple methods of doing so. For example, if we wish to find a size $4 \times 4 = 16$ model of the network, we can do so by dividing the full 16×16 network into $4 \times 4 = 16$ smaller 4×4 -sized blocks and then abstracting each of these blocks, and also by first abstracting $8 \times 8 = 64$ of smaller 2×2 -sized blocks resulting in a size $8 \times 8 = 64$ system, followed by abstracting 16 of smaller 2×2 -sized blocks comprising the size 64 system obtained in the previous step. Note that these abstraction paths can also be completely described by writing down the abstraction points

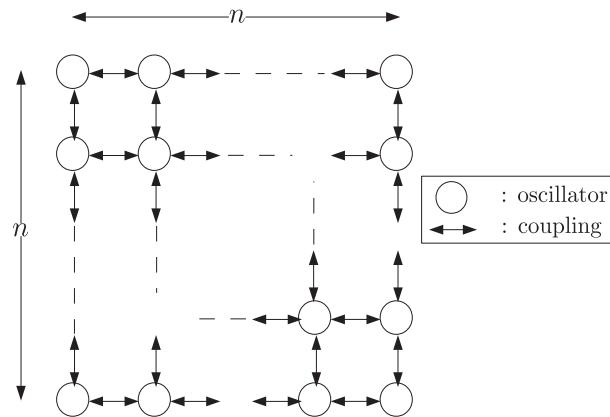


Figure 3. Example of a grid-type coupled oscillator network: an $n \times n$ grid of oscillators, each coupled to its nearest neighbours.

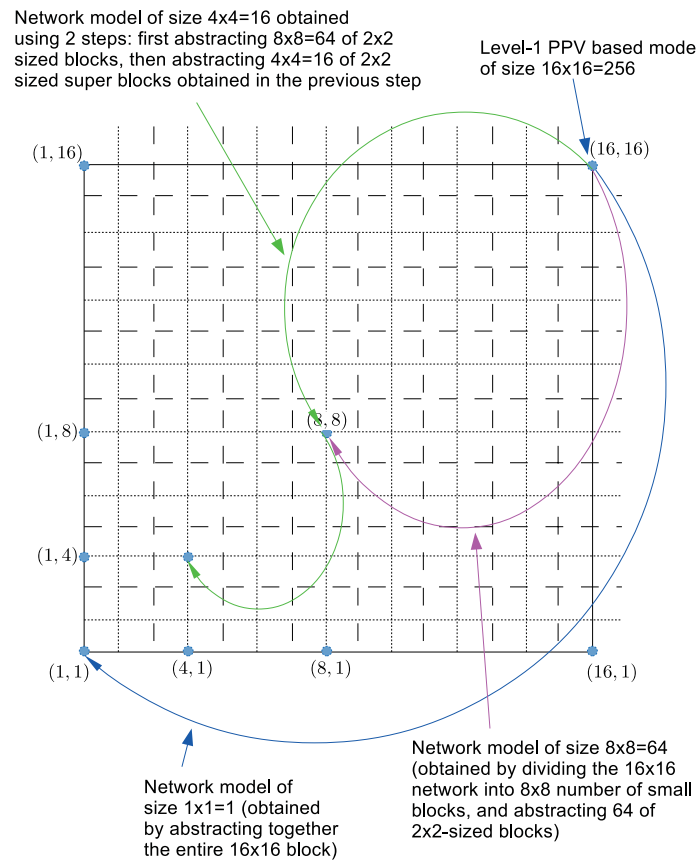


Figure 4. Different abstraction paths for obtaining different sized reduced order models of the network. The figure also shows multiple ways of arriving at the same sized reduced order model.

along the path in order. For example, the first method we mentioned for obtaining a size 16 network model can be written as $(16, 16) \rightarrow (4, 4)$, whereas the second two-step method mentioned can be written as $(16, 16) \rightarrow (8, 8) \rightarrow (4, 4)$. We will find later that different abstraction paths require different computational times and result in varying accuracies of the network model obtained. Also

note that all accuracy is measured relative to the (16, 16) model (it being the most accurate and also computationally the most expensive).

4.1. Ring oscillators

Let us start with a network of ring oscillators, with resistive inter-oscillator coupling. A DAE description of this network is described in what follows.

$$\begin{aligned}
 C_i \frac{d}{dt} x_{i,1}(t) + I_{Dn}(x_{i,3}, x_{i,1}) + I_{Dp}(x_{i,3} - V_{DD}, x_{i,1} - V_{DD}) + \frac{x_{i,1}}{Rn_i} + \frac{x_{i,1} - V_{DD}}{Rp_i} \\
 + \frac{x_{i,1}(t) - x_{i+1,1}(t)}{R_c} + \frac{x_{i,1}(t) - x_{i-1,1}(t)}{R_c} = 0, \\
 C_i \frac{d}{dt} x_{i,2}(t) + I_{Dn}(x_{i,1}, x_{i,2}) + I_{Dp}(x_{i,1} - V_{DD}, x_{i,2} - V_{DD}) + \frac{x_{i,2}}{Rn_i} + \frac{x_{i,2} - V_{DD}}{Rp_i} = 0, \text{ and,} \\
 C_i \frac{d}{dt} x_{i,3}(t) + I_{Dn}(x_{i,2}, x_{i,3}) + I_{Dp}(x_{i,2} - V_{DD}, x_{i,3} - V_{DD}) + \frac{x_{i,3}}{Rn_i} + \frac{x_{i,3} - V_{DD}}{Rp_i} = 0, \text{ for} \\
 i = \{0, 1, 2, 3\}, \quad (78)
 \end{aligned}$$

where $I_{Dn}(V_{GS}, V_{DS})$ is the drain current flowing through the NMOS transistor (similarly I_{Dp} for PMOS transistor) and the subscript indices are to be taken modulo 4. \vec{x}_i 's are the state variables of this oscillator, and is a size-3 vector $[x_{i,1}, x_{i,2}, x_{i,3}]^T$. The model used for the transistors is Shichman–Hodges with $\beta_N = \beta_P = 2 \cdot 10^{-3}$, $V_{TN} = V_{TP} = 0.25\text{V}$, $Rn_i = Rp_i = 10^5 \Omega$, $V_{dd} = 1.2\text{V}$, and $C_i \approx 100\text{nF}$. The capacitance C_i will be varied slightly across the network components.

The aforementioned DAE description is for a 2×2 -sized sub-network. The full 16×16 network is constructed by repeating these 2×2 blocks spatially 64 times, and maintaining the same R_c -resistive coupling topology as is shown in Figure 3.

4.1.1. Identifying the inter-oscillator coupling terms. The inter-coupling term \vec{b}_{ij} for capturing the effect of the j^{th} oscillator on the i^{th} oscillator is given by $\vec{b}_{ij} = \frac{x_{p_{i,1}}(\phi_i(t)) - x_{p_{j,1}}(\phi_j(t))}{R_c}$, $[0, 0]^T$, where $\vec{x}_{p_i} = [x_{p_{i,1}}, x_{p_{i,2}}, x_{p_{i,3}}]^T$ is the one-periodic version of the PSS waveform of the i^{th} oscillator without coupling, provided that oscillators i and j are neighbours (according to the nearest neighbour coupling rule as is shown in Figure 3); else, there is no coupling between them.

4.1.2. Choosing the parameters of the component oscillators. We make the network oscillators slightly different by, say, varying C_i values slightly across the oscillators of the 2×2 repeating block such that the network still locks (Figure 5). Also, we need to enforce the condition of relatively small disturbances $\vec{b}_i(t)$, which includes couplings \vec{b}_{ij} , by choosing R_c appropriately. The magnitudes of the current flowing through the capacitor and transistors at any node is $\approx 1\text{ mA}$. When the oscillators are locked, we expect $|x_{i,k}(t) - x_{j,k}(t)|$ to be $\leq 0.1\text{ V}$ (the voltage swing at any node $x_{i,k}$ is $\approx 1\text{ V}$,

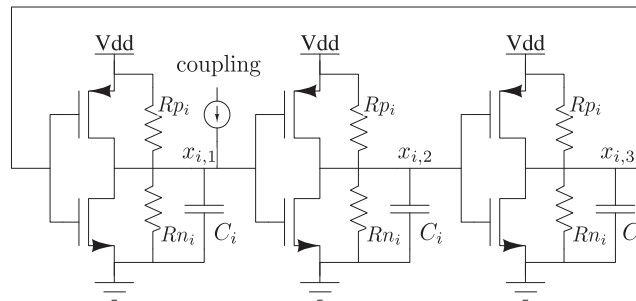


Figure 5. Component ring oscillators of the 16×16 network with point of coupling shown.

because we are dealing with inverters). Thus, $0.1/R_c \ll 10^{-3} \Rightarrow 100 \ll R_c$, and we choose $R_c = 10^4 \Omega$.

4.1.3. Extracting $\vec{x}_p(t)$ waveforms and PPVs of the network components. We use harmonic balance (HB) to extract the PSS waveforms (Figure 6), the natural frequency, and the PPVs (Figure 7) of each of the 4 component oscillators of the 2×2 sub-block, directly from their DAE descriptions. The PPV extraction procedure of [44] is used. We can see (Figures 6 and 7) that the shapes of the PSS and PPV waveforms, and the natural frequencies of the four different types of oscillators are almost identical. This is because the capacitance parameter is only varied slightly, as we want to study weak coupling.

4.1.4. Extracting the locked phase of the network. These component PPVs, along with the inter-component coupling information, are then used to obtain the derivo-periodic solution $\vec{\phi}^*$, and the locked frequency f_g , of the coupled system, again using HB (Figure 8).

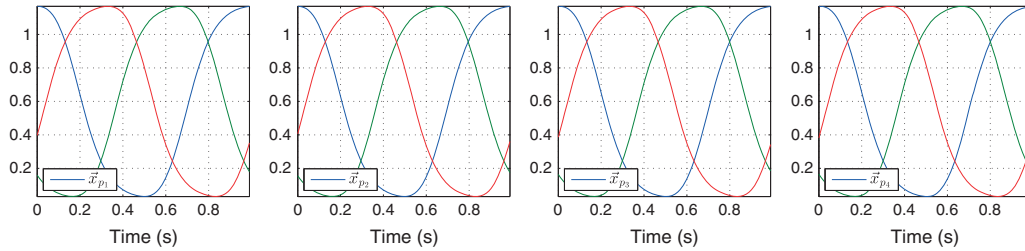


Figure 6. \vec{x}_{p_i} : one-periodic versions of the periodic steady state waveforms of the component ring oscillators that make up the 2×2 repeating block. Their natural frequencies are found to be 1.3614, 1.3478, 1.3753 and 1.3895 KHz (corresponding to C_i values of 99, 100, 98 and 97 nF, respectively).

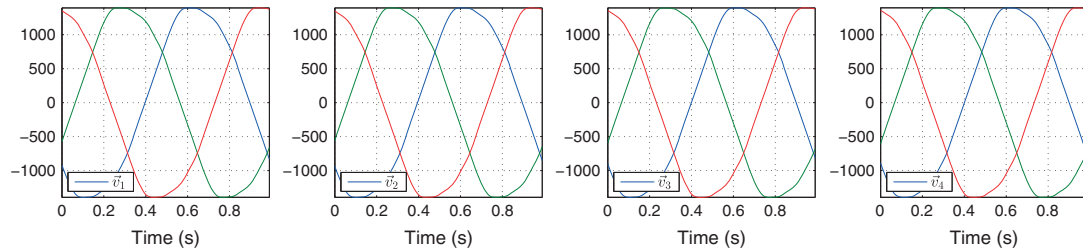


Figure 7. \vec{v}_i : one-periodic version of the PPVs of the component ring oscillators of the 2×2 repeating block.

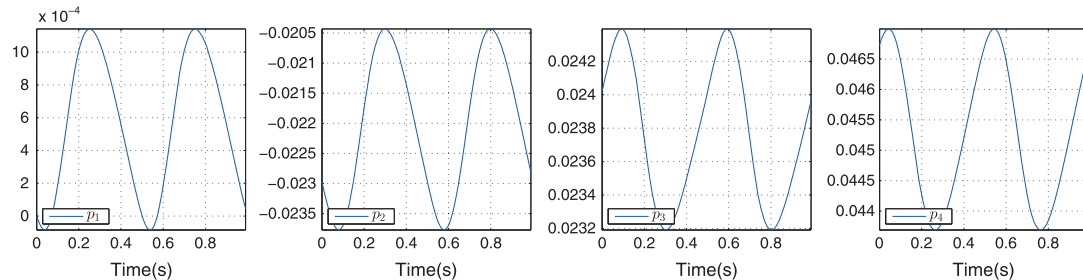


Figure 8. \vec{p} : one-periodic version of the periodic part of the locked phase $\vec{\phi}^*$ computed just for the 2×2 repeating block. Locked frequency is found out to be 1.3693 KHz (same as full simulation based locked frequency).

4.1.5. Abstracting the network as a single oscillator. We now abstract the network as a single oscillator, that is, obtain a size-1 model for it. This is carried out using two different procedures. One is the single-level $(16, 16) \rightarrow (1, 1)$ abstraction path, and the other is the four-level $(16, 16) \rightarrow (8, 8) \rightarrow (4, 4) \rightarrow (2, 2) \rightarrow (1, 1)$ abstraction path. Comparison of locked phase and locked-frequency-scaled coefficient of the disturbance terms $\bar{a}(t)$ in the final abstracted PPV equation obtained using the different procedures can be seen in Figures 9 and 10.

4.1.6. Speedup: comparison of the different network abstraction paths. Note that once the network macromodel has been obtained, all PPV-based simulations take equal time irrespective of the way

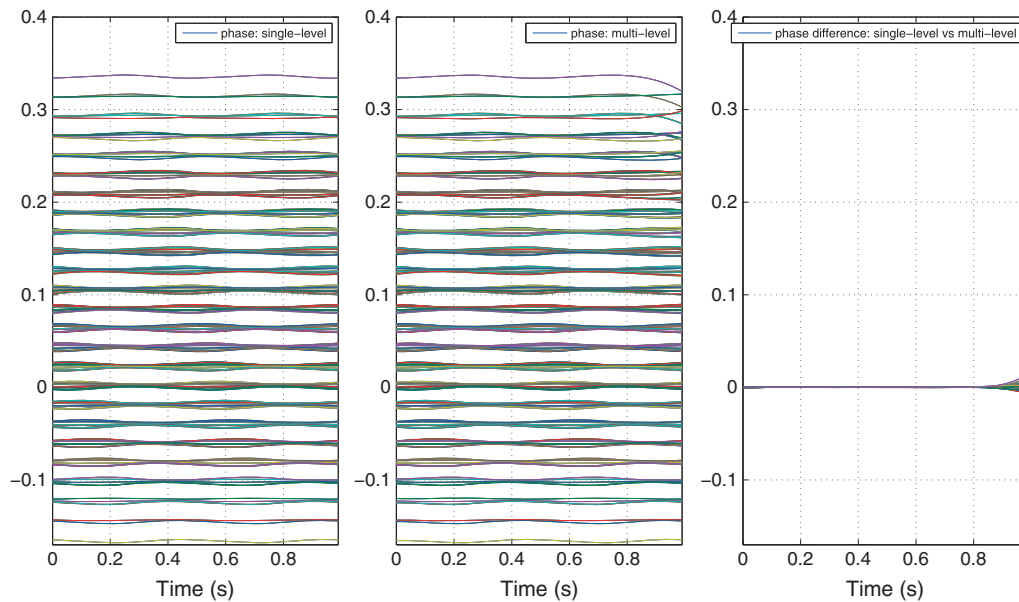


Figure 9. Comparison of 16×16 network's phase computed using single-level versus multi-level approach. Relative error of $5.34 \cdot 10^{-4}$ in the multi-level procedure's result compared to the single-level result.

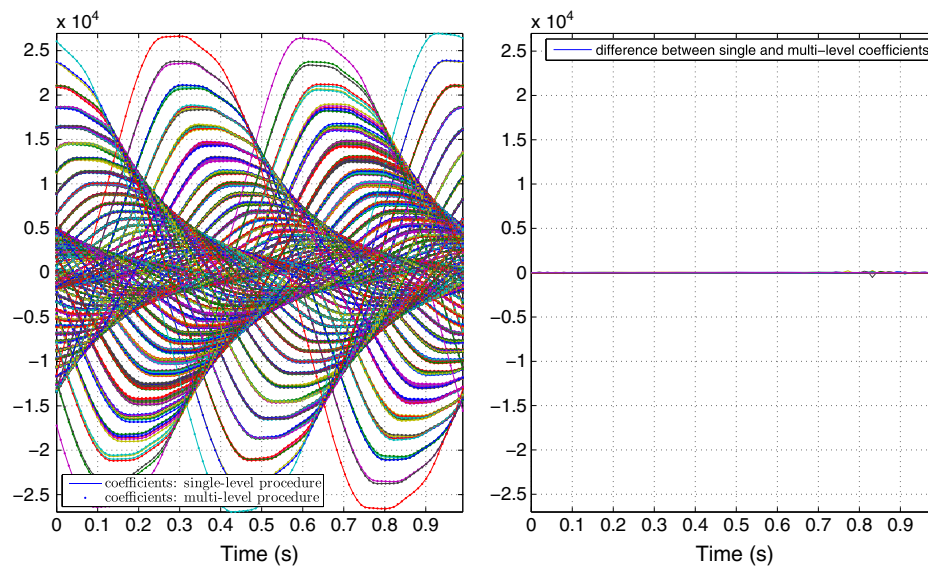


Figure 10. Comparison of 16×16 network's coefficients computed using single-level versus multi-level approach. Relative error of $8.92 \cdot 10^{-4}$ in the multi-level result compared to the single-level result.

(abstraction path) the macromodel was obtained. Also, the natural frequencies, PSS waveforms and PPVs of all the elemental oscillators need to be computed in all PPV-based approaches. Thus, we compare the total time required in computing the network macromodel, given the macromodels of the elemental oscillators, using the single-level versus the multi-level approach for a $2^k \times 2^k$ network composed of all distinct oscillators (unlike Figure 11 network, which is composed of identical 2×2 blocks) (Table I). The table shows a speedup of an order of magnitude when using the multi-level hierarchical procedure as opposed to the single-level hierarchical approach. Note that the speedups would be greater if the network were composed of identical sub-blocks instead (as in Figure 11) because of the time saved in re-abstrating the sub-blocks (Table II). Thus, by imposing a hierarchical structure on a network, we have demonstrated how the multi-level hierarchical procedure can be used to obtain the phase macromodel of *any* CON in significantly lesser time.

4.2. Oscillatory neurons

We now move on to networks of neurons. Neurons in their oscillatory mode can be described using the FitzHugh–Nagumo model in what follows.

$$\begin{aligned} \frac{d}{dt}x_1 &= x_1 - x_1^3 - x_2 + I_{ext} + D_1 \nabla^2 x_1, \text{ and,} \\ \tau \frac{d}{dt}x_2 &= x_1 + a - b \cdot x_2 + D_2 \nabla^2 x_2, \end{aligned} \quad (79)$$

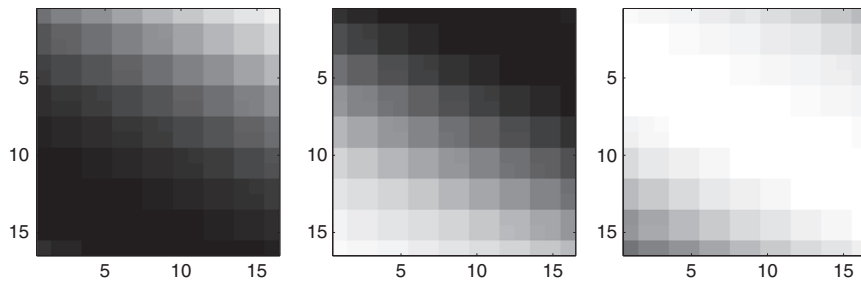


Figure 11. Snapshot of the network waveform $\vec{x}(t)$ for a 16×16 CON computed using the four-level four-at-once procedure. This 16×16 network is composed iteratively using identical 2×2 blocks of the 2×2 network used earlier in this section.

Table I. Time required in computing the network macromodel using single-level and k-level multi-level methods ($k = 1, 2, 3, 4, 5, 6$) for different network sizes ($2^k \times 2^k$).

System size	2×2	4×4	8×8	16×16	32×32	64×64
Single-level (s)	2	15	200	3,000	Unknown	Unknown
Multi-level (s)	2	10	43	200	≈ 1500	$\approx 22,000$

Table II. Time required in computing the network model using single-level and k-level multi-level methods for different network sizes ($2^k \times 2^k$).

System size	2×2	4×4	8×8	16×16	32×32	64×64
Single-level (s)	2	15	200	3,000	Unknown	Unknown
Multi-level (s)	2	4	7	33	≈ 650	$\approx 16,000$

The networks are constructed by repeating over blocks of the 2×2 network used in Section 4. This makes the $2^{i+1} \times 2^{i+1}$ network composed of 4 identical $2^i \times 2^i$ blocks, $1 \leq i \leq 5$.

where the parameter values are chosen to be $a = 0.5, b = 0, \tau \approx 12.5$, and $I_{ext} = 0.5$, for oscillations to show up. The state variables x_1 and x_2 are functions of time, as well as the spatial coordinates of the system. The parameter τ will be varied slightly across the network.

4.2.1. Identifying the inter-oscillator coupling terms. Equation (79) needs to be discretized spatially in order for it to become amenable to numerical analysis (note that the state variables are discretized along the time coordinate too, but we seldom mention this fact explicitly). The inter-oscillator coupling in the previous equations arises from the Laplacian terms $D_k \nabla^2 x_k, k = 1, 2$ that model the phenomenon of diffusion across the network. These diffusion terms can be discretized as follows:

$$\nabla^2 x_{i,j,k} = \frac{x_{i+1,j,k} + x_{i-1,j,k} - 2x_{i,j,k} + x_{i,j+1,k} + x_{i,j-1,k} - 2x_{i,j,k}}{\Delta h^2}, \quad (80)$$

where Δh stands for one step in space discretization along the horizontal and vertical directions. For boundary points (i, j) , we choose non-flux boundary conditions, that is, $\nabla x_k \cdot \vec{n} = 0$, where \vec{n} is the normal to the boundary. Using these non-flux boundary conditions, the coupling terms at the boundary points can be written as

$$\nabla^2 x_{i,j,k} = \frac{x_{i+1,j,k} + x_{i-1,j,k} - 2x_{i,j,k} + x_{i,j+1,k} - x_{i,j,k}}{\Delta h^2}, \quad (81)$$

for the left vertical boundary; similar for other three boundaries. Now we can clearly see how the discretized version of the diffusion terms, along with the non-flux boundary conditions, models a nearest neighbour resistive coupling (Figure 3) like the one in the previous ring oscillator example.

4.2.2. Choosing the parameters of the network. The effective coupling resistance R_c for this network is given by $\frac{\Delta h^2}{D_k}$. For space discretization step size $\Delta h = 2$, say, and diffusion coefficients $D_1 = D_2 = 0.1$, say, we obtain effective $R_c = 40\Omega$. The PSS waveforms of the individual oscillators are of the order of unity, and thus, diffusion coefficient of one order less seems viable for maintaining the weak coupling condition.

Now we vary the parameter $\tau_{i,j}$ (associated with the oscillator at position (i, j) in the grid) across the network in various ways, so as to obtain a grading across the network:

- If we choose $\tau_{i,j} = 12.5$ for odd columns of the network grid, and $= 12.2$ for even columns, we obtain a network composed of two types of elemental oscillators that alternate along the horizontal direction. We call this grading pattern 'xyxy' because the type of oscillators are alternating along the horizontal direction.
- Similarly, we define an 'xyyx' grading pattern meaning the pattern 'xyyx' repeats along the horizontal direction.
- If we choose $\tau_{i,j}$ to alternate in concentric squares, starting from the centre most 2×2 square, we end up with a radial grading pattern.

4.2.3. Abstracting the network as a single oscillator. The steps for extracting the individual oscillator's PSS waveforms and PPVs are similar to the previous example, and we skip these steps here. Instead, we straightaway have a look at the locked network's waveforms. Figures 12–16 show the snapshots of the locked network's waveform computed using (16, 16) abstraction procedure for the xyxy-graded network. Similarly, Figures 17–26 show the same for the xyyx-graded and the radially graded network, respectively. We observe wavefronts travelling from right to left in the xyxy-graded network. This directional asymmetry in the locked waveform of this network arises from the reflection asymmetry present in the network – namely, the first and last columns of the grid are of different types ('x' vs 'y'). It would be worth mentioning here that the PSS waveform shows waves travelling from left to right if the network is graded in a 'xyyx' pattern instead. It would be expected that if we somehow impose reflection symmetry on the network, the directional nature of the travelling waves should no longer be supported, and, instead, reflection symmetric patterns

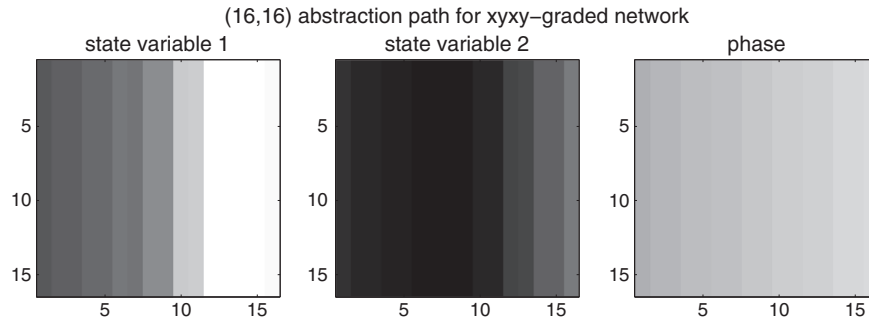


Figure 12. Snapshot of the network waveform $\vec{x}(t)$ at $t = 0$ for a 16×16 xyxy-graded neuron network computed using the $(16, 16) \rightarrow (1, 1)$ procedure.

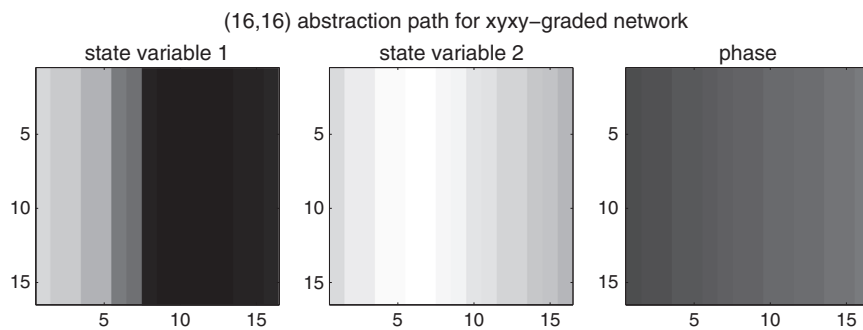


Figure 13. Snapshot of the network waveform $\vec{x}(t)$ at $t = T/5$ for a 16×16 xyxy-graded neuron network computed using the $(16, 16) \rightarrow (1, 1)$ procedure.

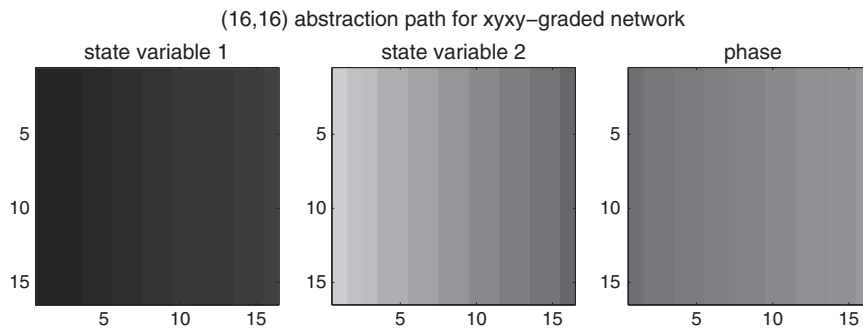


Figure 14. Snapshot of the network waveform $\vec{x}(t)$ at $t = 2T/5$ for a 16×16 xyxy-graded neuron network computed using the $(16, 16) \rightarrow (1, 1)$ procedure.

would emerge. This is indeed true and is observed in the case of ‘xyyx’ grading which makes the network reflection symmetric about the vertical axis. The network now exhibits standing wave patterns (Figures 17–21). Further following the symmetry argument, we observe that radial waves are generated in the PSS solution of a radially graded network, that is, radial symmetry in oscillator distribution across a network does give rise to radially symmetric PSS patterns in the locked network (Figures 22–26).

All the aforementioned networks were abstracted as a single oscillator using the $(16, 16) \rightarrow (1, 1)$ abstraction procedure. Let us examine a different $(16, 16) \rightarrow (8, 8) \rightarrow (4, 4) \rightarrow (2, 2) \rightarrow (1, 1)$, say, abstraction path now. The snapshots of the locked waveforms resulting from this model can be seen in Figures 27–31. Note the coarser wavefronts obtained compared to the

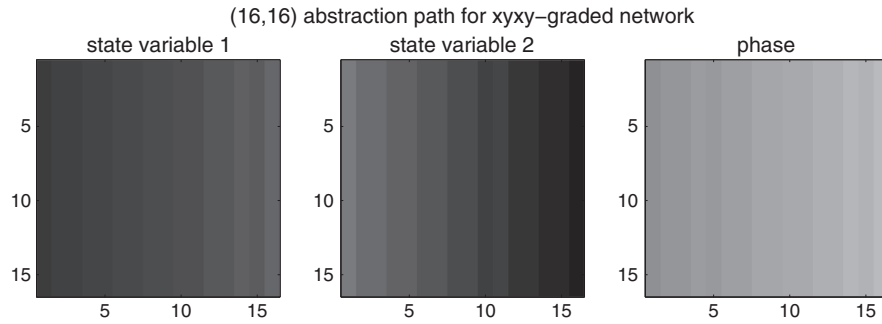


Figure 15. Snapshot of the network waveform $\vec{x}(t)$ at $t = 3T/5$ for a 16×16 xyxy-graded neuron network computed using the $(16, 16) \rightarrow (1, 1)$ procedure.

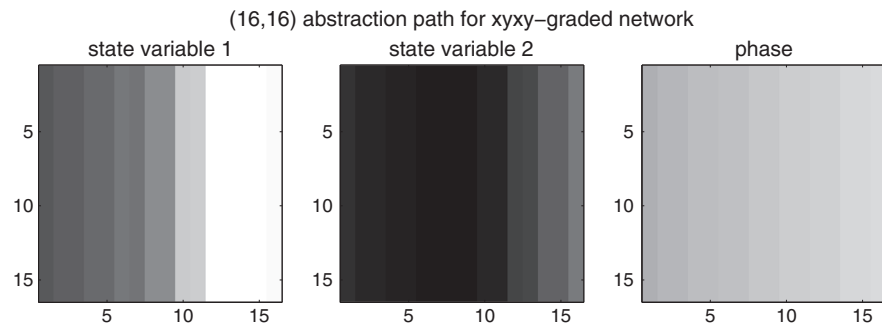


Figure 16. Snapshot of the network waveform $\vec{x}(t)$ at $t = 4T/5$ for a 16×16 xyxy-graded neuron network computed using the $(16, 16) \rightarrow (1, 1)$ procedure.

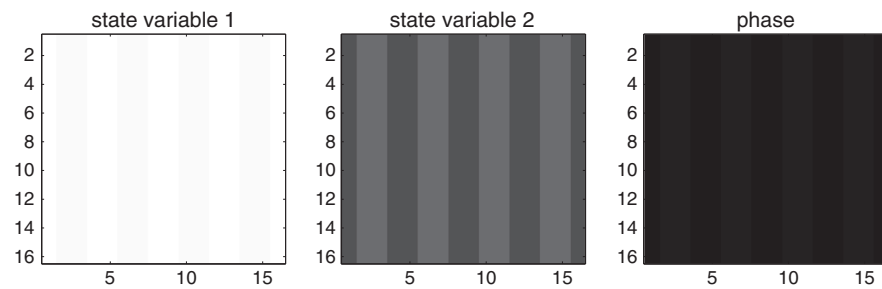


Figure 17. Snapshot of the network waveform $\vec{x}(t)$ at $t = 0$ for a 16×16 xyxy-graded neuron network computed using the $(16, 16) \rightarrow (1, 1)$ procedure.

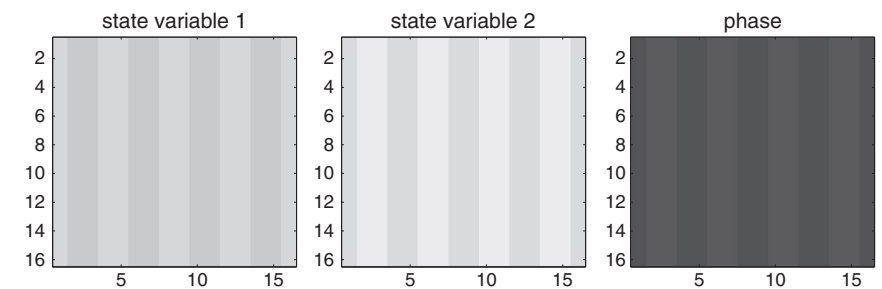


Figure 18. Snapshot of the network waveform $\vec{x}(t)$ at $t = T/5$ for a 16×16 xyxy-graded neuron network computed using the $(16, 16) \rightarrow (1, 1)$ procedure.

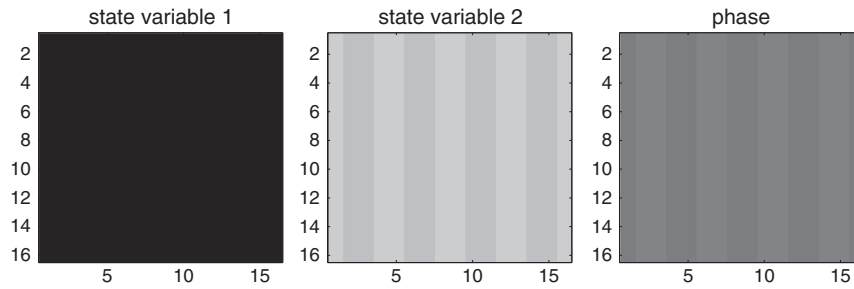


Figure 19. Snapshot of the network waveform $\vec{x}(t)$ at $t = 2T/5$ for a 16×16 xyx-graded neuron network computed using the $(16, 16) \rightarrow (1, 1)$ procedure.

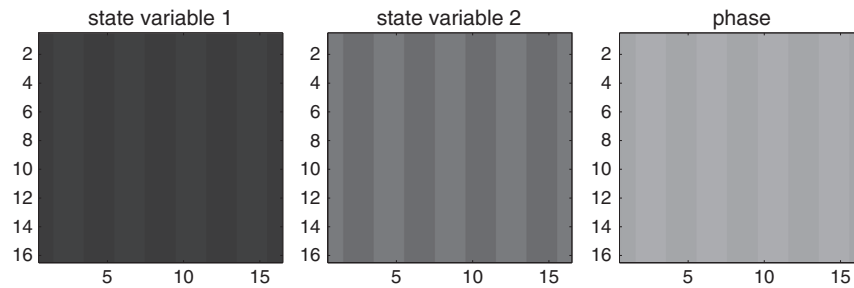


Figure 20. Snapshot of the network waveform $\vec{x}(t)$ at $t = 3T/5$ for a 16×16 xyx-graded neuron network computed using the $(16, 16) \rightarrow (1, 1)$ procedure.

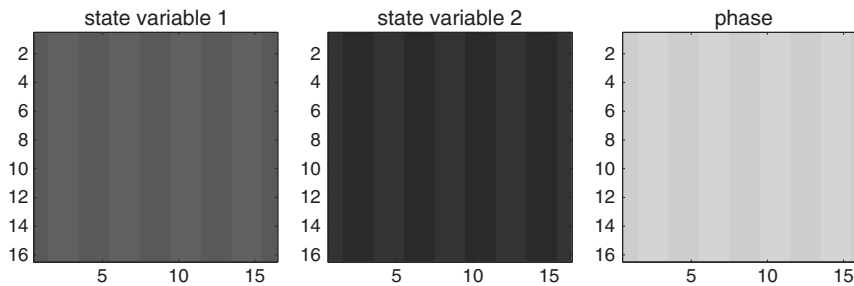


Figure 21. Snapshot of the network waveform $\vec{x}(t)$ at $t = 4T/5$ for a 16×16 xyx-graded neuron network computed using the $(16, 16) \rightarrow (1, 1)$ procedure.

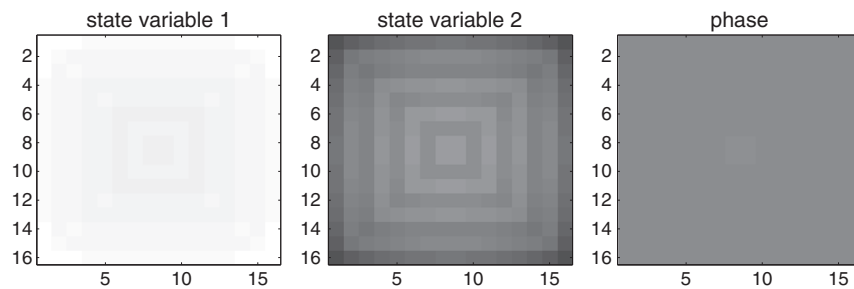


Figure 22. Snapshot of the network waveform $\vec{x}(t)$ at $t = 0$ for a 16×16 radially graded neuron network computed using the $(16, 16) \rightarrow (1, 1)$ procedure.

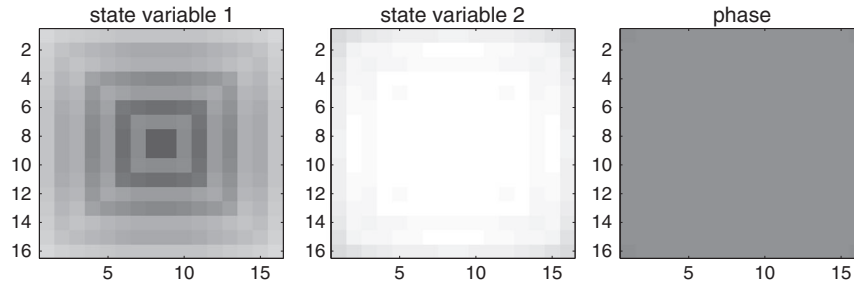


Figure 23. Snapshot of the network waveform $\vec{x}(t)$ at $t = T/5$ for a 16×16 radially graded neuron network computed using the $(16, 16) \rightarrow (1, 1)$ procedure.

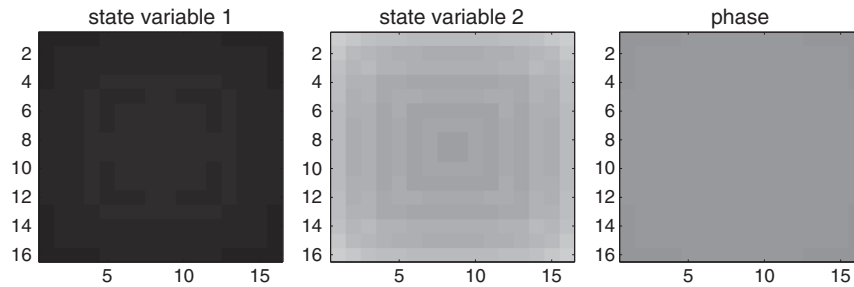


Figure 24. Snapshot of the network waveform $\vec{x}(t)$ at $t = 2T/5$ for a 16×16 radially graded neuron network computed using the $(16, 16) \rightarrow (1, 1)$ procedure.

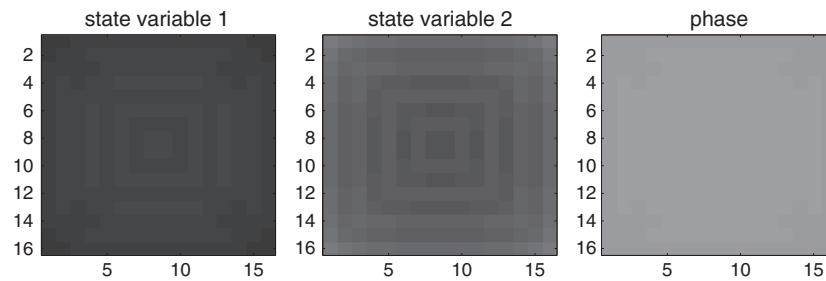


Figure 25. Snapshot of the network waveform $\vec{x}(t)$ at $t = 3T/5$ for a 16×16 radially graded neuron network computed using the $(16, 16) \rightarrow (1, 1)$ procedure.

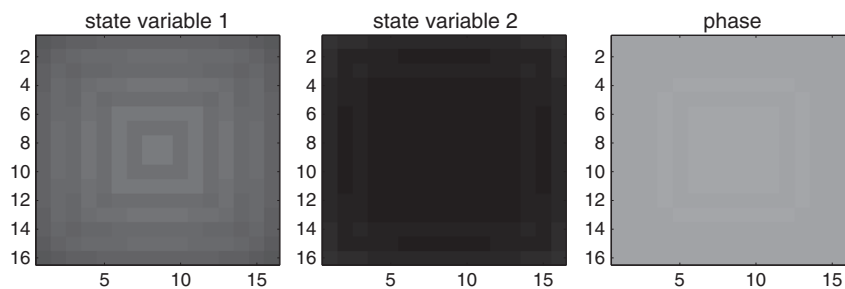


Figure 26. Snapshot of the network waveform $\vec{x}(t)$ at $t = 4T/5$ for a 16×16 radially graded neuron network computed using the $(16, 16) \rightarrow (1, 1)$ procedure.

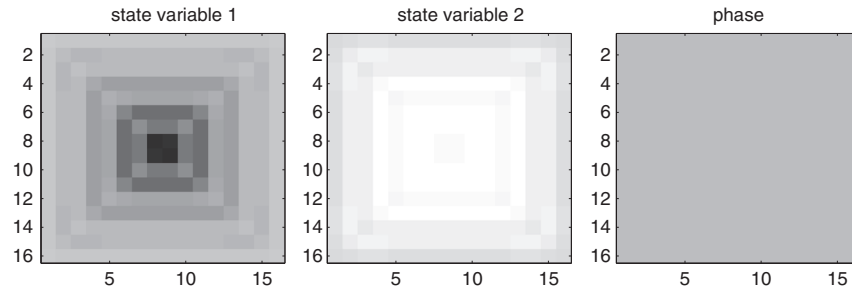


Figure 27. Snapshot of the network waveform $\vec{x}(t)$ at $t = 0$ for a 16×16 radially graded neuron network computed using the $(16, 16) \rightarrow (8, 8) \rightarrow (4, 4) \rightarrow (2, 2) \rightarrow (1, 1)$ procedure.

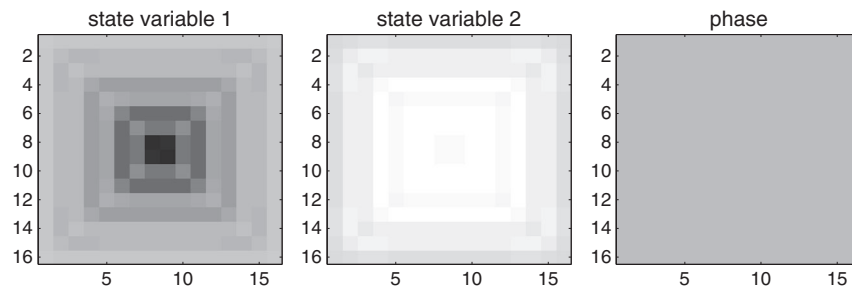


Figure 28. Snapshot of the network waveform $\vec{x}(t)$ at $t = T/5$ for a 16×16 radially graded neuron network computed using the $(16, 16) \rightarrow (8, 8) \rightarrow (4, 4) \rightarrow (2, 2) \rightarrow (1, 1)$ procedure.

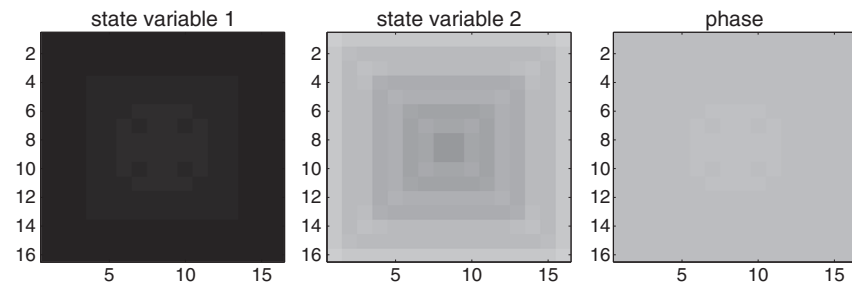


Figure 29. Snapshot of the network waveform $\vec{x}(t)$ at $t = 2T/5$ for a 16×16 radially graded neuron network computed using the $(16, 16) \rightarrow (8, 8) \rightarrow (4, 4) \rightarrow (2, 2) \rightarrow (1, 1)$ procedure.

$(16, 16) \rightarrow (1, 1)$ procedure. Figure 32 shows the plots of the abstracted PPVs obtained after each level of abstraction in the aforementioned multi-level procedure. Note that the locked phase solution obtained in the reduced order system is mapped back to the phase of the state space variables because our aim was to find the locked waveforms of the network. This is carried out by going in the reverse direction of the abstraction path, and iteratively finding the locked phase of the four lower-level components (starting from $(1, 1)$ and going up to $(16, 16)$).

4.2.4. Speedup: single-level versus multi-level. Table III shows the speedup obtained when using the multi-level approach when abstracting radially graded networks of different sizes. A speedup of up to two orders of magnitude is observed.

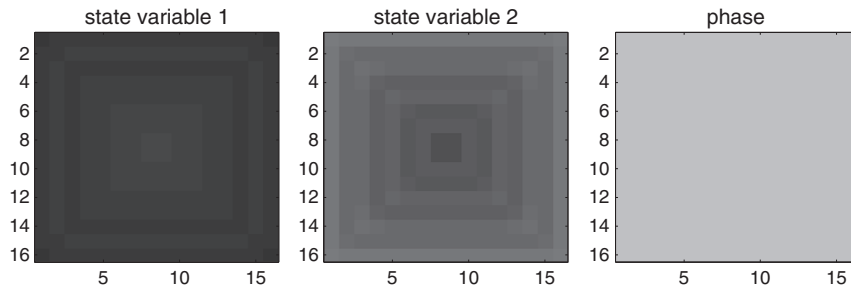


Figure 30. Snapshot of the network waveform $\vec{x}(t)$ at $t = 3T/5$ for a 16×16 radially graded neuron network computed using the $(16, 16) \rightarrow (8, 8) \rightarrow (4, 4) \rightarrow (2, 2) \rightarrow (1, 1)$ procedure.

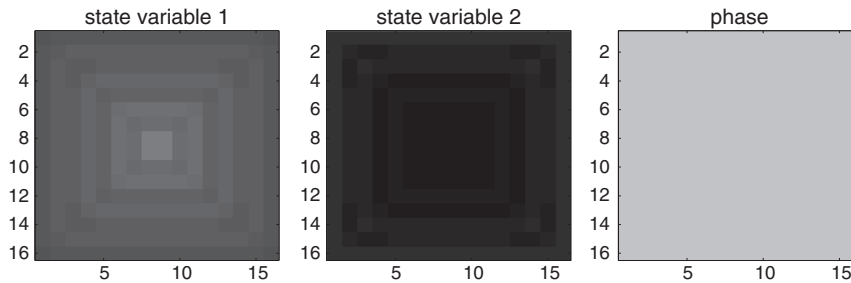


Figure 31. Snapshot of the network waveform $\vec{x}(t)$ at $t = 4T/5$ for a 16×16 radially graded neuron network computed using the $(16, 16) \rightarrow (8, 8) \rightarrow (4, 4) \rightarrow (2, 2) \rightarrow (1, 1)$ procedure.

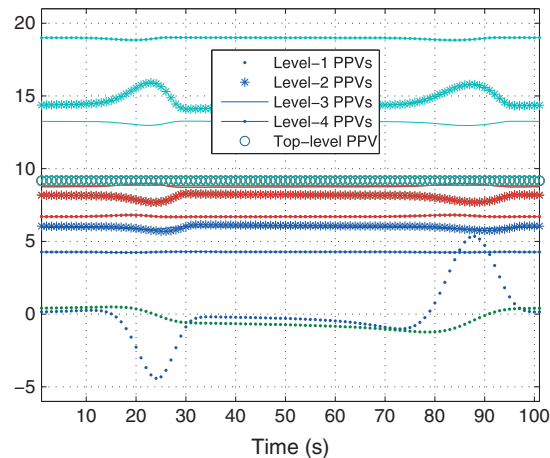


Figure 32. Plot of the abstracted PPVs obtained at each level when using the multi-level abstraction procedure $(16, 16) \rightarrow (8, 8) \rightarrow (4, 4) \rightarrow (2, 2) \rightarrow (1, 1)$.

4.3. Mechanical pendulum clocks

As our third illustrative example, we use mechanical clocks for the individual oscillators. Each clock is modelled as a nonlinear mechanical pendulum with friction-based damping, together with a position-dependent, impulse-like, autonomous restoring force (representing, e.g. the spring-powered ratchet mechanism that sustains mechanical clocks and watches) that makes the pendulum self-sustaining. The differential equation describing each self-sustaining pendulum is

Table III. Time required in computing the network macromodel using single-level and multi-level procedures for radially graded network of different sizes.

System size	2×2	4×4	8×8	16×16
Single-level (s)	20	253	14619	52290
Multi-level (s)	19	160	422	2616

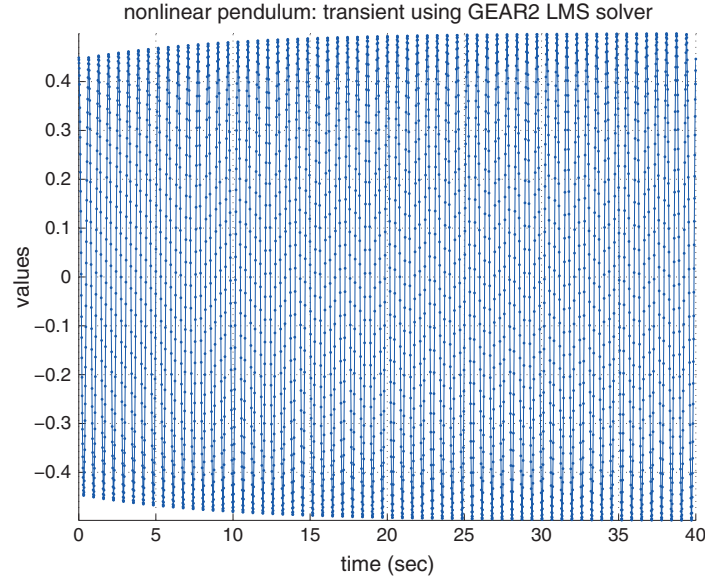


Figure 33. Transient simulation of pendulum clock, showing amplitude stabilization of $\theta(t)$.

$$\frac{d^2\theta}{dt^2} = -\frac{g}{l} \sin(\theta) - \underbrace{d \frac{l}{m} \frac{d\theta}{dt}}_{\text{damping}} + \underbrace{\frac{A}{m} \sqrt{\frac{k_1}{\pi}} e^{-k_1(\theta-\theta_0)^2} \tanh\left(k_2 \frac{d\theta}{dt}\right)}_{\text{impulse-like restoring force}} + \frac{f_{\text{ext}}(t)}{m}. \quad (82)$$

In the previous discussion, $\theta(t)$ is the angle of the pendulum's string from the vertical (in radians); $g = 9.81 \text{ m/s}^2$ is the gravitational acceleration at the Earth's surface; $l \simeq 0.1 \text{ m}$ is the length of the pendulum's string; $d = 0.1$ is the coefficient of damping due to friction; $m = 0.1 \text{ kg}$ is the mass of the pendulum; A , set to $2ld$, is a parameter representing the peak value of the autonomous restoring force (in Newtons); $k_1 = 40$ is a parameter that determines how impulsive the restoring force is; $\theta_0 = 0$ is the angle at which the restoring force kicks in; $k_2 = 1$ is a parameter that controls how rapidly the restoring force saturates as a function of the velocity of the pendulum; and $f_{\text{ext}}(t)$ is an externally applied force, nominally set to 0. To conform to the theory presented in the previous section, (82) is written (and implemented in our code) as the size-2 system of first-order differential equations

$$\begin{aligned} \frac{dv_\theta}{dt} &= -\frac{g}{l} \sin(\theta) - \underbrace{d \frac{l}{m} \frac{d\theta}{dt}}_{\text{damping}} + \underbrace{\frac{A}{m} \sqrt{\frac{k_1}{\pi}} e^{-k_1(\theta-\theta_0)^2} \tanh\left(k_2 \frac{d\theta}{dt}\right)}_{\text{impulse-like restoring force}} + \frac{f_{\text{ext}}(t)}{m}, \\ \frac{d\theta}{dt} &= v_\theta. \end{aligned} \quad (83)$$

Figure 33 depicts $\theta(t)$ obtained by transient simulation of (83) with parameters as noted previously, no external force, and initial condition $[\theta(0), v_\theta(0)] = [\frac{\pi}{7}, 0]$. It can be seen that the

amplitude stabilizes as time progresses. The precise steady state waveform was obtained from HB simulation using 10 harmonics; the results are depicted in Figure 34(a). The steady state is almost a perfect sinusoid, as can be seen from the very small higher-harmonic content; the period of the steady state waveform is 0.64486 s (i.e. frequency 1.5507 Hz), as found by HB. The PPV of the external input $f_{\text{ext}}(t)$, extracted via the HB adjoint method described in [44], is shown in Figure 34(b) – it can be seen that this, too, is very sinusoidal.

To build the coupled network, we introduced weak coupling between neighbouring oscillators in the rectangular grid. The coupling was modelled as weak springs between the pendulums, resulting in an external force $f_{\text{ext}}(t)$ on each oscillator that depended on the instantaneous positions of its neighbours relative to its own. As described in the previous section, the network was built up hierarchically, starting at the bottom with a 2×2 block of oscillators (each with a slightly different string length, resulting in slightly different natural frequencies: 1.55071418, 1.549952395, 1.5514771049 and 1.549952395 Hz, respectively). Four of these 2×2 oscillator blocks were then coupled in a higher-level 2×2 grid to form a 4×4 grid of elemental oscillators; and so on for two more levels, to obtain a 16×16 grid of oscillators. With reference to Figure 4, the network was abstracted hierarchically via the $(16, 16) \rightarrow (8, 8) \rightarrow (4, 4) \rightarrow (2, 2) \rightarrow (1, 1)$ abstraction path, to arrive at a single PPV model for the entire network 16×16 network.

Once the elemental oscillators' PPVs were extracted, it was easy and quick to explore the effect of different couplings on the (locked) phase patterns of the network, simply by re-doing hierarchical abstraction starting from the elemental oscillators' PPVs. Figure 35(a) illustrates lock patterns in the network of oscillators for our nominal value of weak coupling (normalized to 1). The two figures depict instantaneous magnitudes of $\theta(t)$ and $v_\theta(t)$, respectively, across all oscillators in the network. Observe that all oscillators across the network have almost the same magnitude, indicating that the

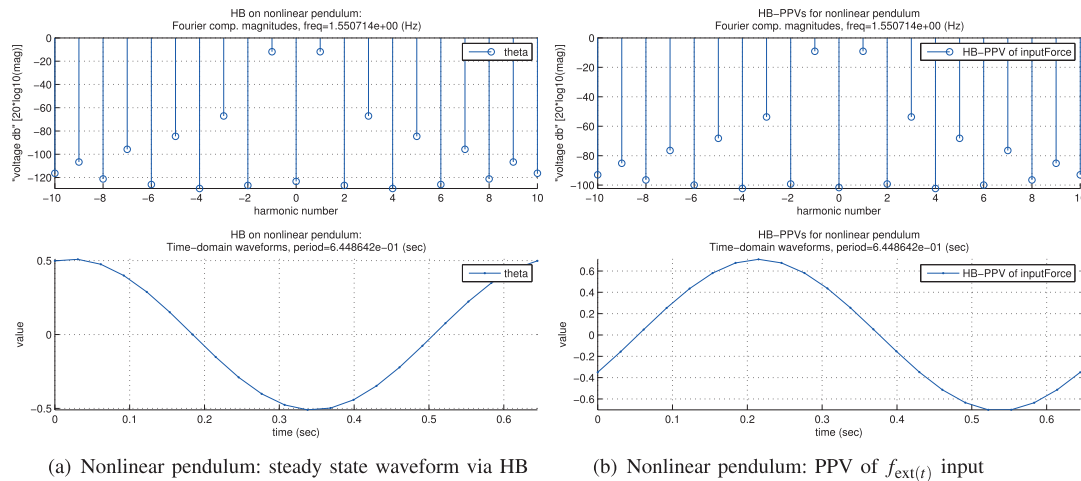


Figure 34. Nonlinear pendulum: steady state and Perturbation Projection Vector (PPV) waveforms/harmonics.

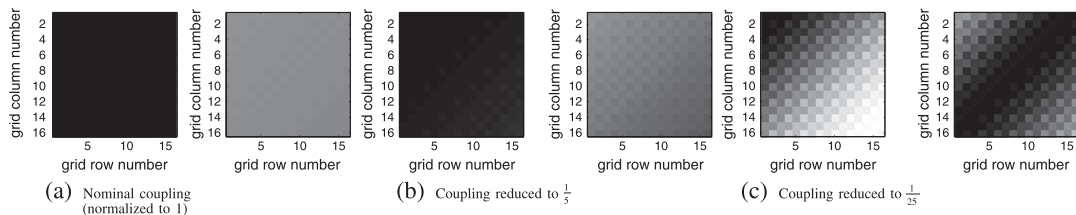


Figure 35. Snapshots of oscillator $\theta(t)$ and $v_\theta(t)$ for a 16×16 coupled oscillator network of pendulum oscillators for three different values of weak coupling. This 16×16 network is composed hierarchically using identical 2×2 superblocks of 2×2 blocks of elemental pendulum oscillators.

phase differences between them are small – that is, all the pendulums are swinging in almost exactly the same phase.

When the coupling is weakened by a factor of 5, the phase patterns change, as shown in Figure 35(b). Note that there is an average variation in magnitude as we go from the top left to the bottom right, indicating a gradual diagonal phase shift. A closer look also reveals seemingly identical local patterns in each 2×2 block – this is, of course, because the elemental oscillators in each such block are heterogenous, with identical blocks repeated to build the network. When the coupling is reduced further by another factor of 5, the differences in instantaneous phase across the network become even more apparent, as seen in Figure 35(c). However, the network still remains phase locked, which implies, of course, that all the pendulums are oscillating at the same frequency (in this case 1.55052386057 Hz, as computed by our method), although in very different relative phases.

4.4. Time complexity of different abstraction paths

Here we explore the time complexity of the single and multi-level abstraction procedures on networks with different topologies.

Let $T(x, y)$ be the runtime of the abstraction procedure for a network composed of x blocks, each of size y (i.e. having y number of state variables). These state variables are needed for computing the coupling function of each block and we will soon find out that this number depends on the network connectivity (or, topology). Let the size of the network under consideration be $n = 4^k$, for some $k \in \mathbb{N}_0$. Then, because the $2^k \times 2^k$ network is composed of 4^k smaller 1×1 -sized blocks, its time complexity will be given by $T(4^k, n_s \cdot 1)$, where n_s is the number of state variables present in a single elemental oscillator, and is a constant. Now let us try to write down the time complexity of the multi-level procedure corresponding to the path $(2^k, 2^k) \rightarrow (2^{k-1}, 2^{k-1}) \rightarrow \dots \rightarrow (2, 2) \rightarrow (1, 1)$. The first step consists of abstracting 4^{k-1} of 2×2 blocks, each block having $4 \cdot n_s$ number of state variables. Similarly, the i^{th} -step consists of abstracting 4^{k-i} of 2×2 blocks, each block having $4^i \cdot n_s$ number of state variables. Thus, the time complexity for this abstraction path can be given by the sum,

$$\sum_{i=1}^k T(4, 4^i \cdot n_s) \cdot 4^{k-i}. \quad (84)$$

We now move on towards finding the individual $T(x, y)$ terms used previously.

Systems of the form $(HB \text{ matrix}) \cdot a = b$ needs to be solved for at each step of the Newton–Raphson (NR) procedure used for solving the HB system. It is a good approximation to assume that NR takes $O(1)$ number of steps to converge to a solution. The size of the HB matrix corresponding to $T(x, y)$ is $n_h x$, where n_h is the number of harmonics to be solved for and is generally a constant. The cost for solving $(HB \text{ matrix}) \cdot a = b$ is $O((n_h x)^2)$ if the HB matrix is sparse; else, it is $O((n_h x)^3)$.

4.4.1. Time complexity of the multi-level procedure. The size of the HB matrix is $4n_h$ for the multi-level procedure being considered here. This is a constant, and thus, solving the linear system at each step of NR takes constant time. The main cost now becomes evaluating the HB matrix from the coupling function. Conversions to and from time domain to frequency domain require $O(n_h \log(n_h)) = O(1)$ time. Computing the Jacobian of the coupling function at the i^{th} -step takes $O(2^i)$ time if the coupling is sparse; else, it takes $O(4^i \cdot 4^i) = O(4^{2i})$ time for densely connected networks. Thus, for sparsely connected networks, the time complexity turns out to be

$$\sum_{i=1}^k O(2^i) \cdot 4^{k-i} = O\left(\sum_{i=1}^k 2^{2k-i}\right) = O\left(2^{2k} \sum_{i=1}^k 2^{-i}\right) = O(4^k) = O(n), \quad (85)$$

whereas for densely connected networks, the complexity can be given by

$$\sum_{i=1}^k O(4^{2i}) \cdot 4^{k-i} = O\left(\sum_{i=1}^k 4^{k+i}\right) = O\left(4^k \sum_{i=1}^k 4^i\right) = O(4^{2k}) = O(n^2). \quad (86)$$

Now suppose that the network is composed of identical oscillators with identical couplings (or, equivalently, is composed of repeating sub-blocks of constant size forming the entire network). The factor of 4^{k-i} in (84) drops off because all 4^{k-i} of the sub-networks are identical and we need to only compute the abstraction once. Thus, for sparsely connected networks composed of identical oscillators and with symmetrical coupling, the time complexity is given by

$$\sum_{i=1}^k O(2^i) = O\left(\sum_{i=1}^k 2^i\right) = O(2^k) = O(\sqrt{n}). \quad (87)$$

whereas for densely connected networks, this complexity is

$$\sum_{i=1}^k O(4^{2i}) = O(4^{2k}) = O(n^2). \quad (88)$$

4.4.2. Time complexity of the single-level procedure. Turning back to the single-level procedure, we notice that the size of the HB matrix corresponding to $T(4^k, n_s)$ is no longer constant but $n_h 4^k$. The time required in computing the Jacobian of the coupling function to be used for computing the HB matrix is $O(2^k)$ if the network is sparse; else it is $O(4^{2k})$ for dense networks. Also, the time required in solving the linear system associated with NR iteration is $O(4^{2k})$ if the network and, thus, the HB matrix is sparse; else, it is $O(4^{3k})$. Thus, for sparsely connected networks, the time complexity of the single-level approach is $O(4^{2k}) = O(n^2)$, whereas it is $O(4^{3k}) = O(n^3)$ for densely connected networks. The complexity for networks composed of identical oscillators and couplings is the same because the single-level procedure cannot exploit the structure of the network.

Thus, in this section, we have provided an argument showing that the multi-level procedure is far more efficient compared to the single-level procedure by at least a factor of $O(n)$. Also, the multi-level approach is seen to be capable of exploiting the structural symmetry of the network, whereas the single-level approach cannot.

5. CONCLUSION

It is impractical to use brute force simulation methods based on the DAE description of systems to predict the behaviour of large CONs. Hence, reduced order models have been used in the literature, PPV-based macromodels being one of the well-known ones. Here we propose methods based on PPVs to abstract a synchronized network of coupled oscillators as a single oscillator. Our method can be used to abstract networks composed of networks of oscillators themselves.

Here we see that we can either abstract an entire network at once (single-level method) using the theory proposed, or we can go about it in steps abstracting only a few sub-networks at any given step (multi-level). It was shown in this paper that extracting reduced order PPV-based macromodels in a single-level fashion can be very costly for large networks. Thus, we use multi-level procedures, which are seen to be almost as accurate as the single-level methods, but with a speedup factor of $O(N)$ at least (N is the network size). Our technique exploits the structural information (e.g. symmetries and sparse connectivity) present in the network to *hierarchically* extract the network macromodel in a computationally efficient and accurate way.

ACKNOWLEDGEMENT

We would like to thank the anonymous reviewers for their careful reading of the manuscript.

REFERENCES

1. Hodgkin AL, Huxley AF. A quantitative description of membrane current and its application to conduction and excitation in nerve. *The Journal of Physiology* August 1952; **117**:500–544.
2. FitzHugh F. Impulses and Physiological States in Theoretical Models of Nerve Membrane. *Biophysical Journal* July 1961; **1**:445–466.
3. Lai X, Roychowdhury J. Analytical equations for predicting injection locking in LC and ring oscillators. *Proceedings of IEEE CICC*, San Jose, CA., 18–21 Sept. 2005; 461–464.
4. Adler R. A study of locking phenomena in oscillators. *Proceedings of the IEEE* 1973; **61**:1380–1385. Reprinted from [53].
5. Bhansali P, Roychowdhury J. Gen-Adler: the generalized Adler's equation for injection locking analysis in oscillators. *Proceedings of IEEE ASP-DAC*, Taipei, Taiwan, January 2009; 522–227.
6. Armand M. On the output spectrum of unlocked driven oscillators. *Proceedings of the IEEE* May 1969; **57**:798–799.
7. Demir A, Gu C, Roychowdhury J. Phase equations for quasi-periodic oscillators. In *2010 IEEE/ACM International Conference on Computer-Aided Design (ICCAD)*. IEEE: San Jose, 2010; 292–297.
8. Bick C, Timme M, Paulikat D, Rathlev D, Ashwin P. Chaos in Symmetric Phase Oscillator Networks. *Physical Review Letters* December 2011; **107**(24):244101.
9. Strogatz S. *Sync: The Emerging Science of Spontaneous Order*. Theia: Hyperion, March 2003.
10. Panfilov AV, Holden AV. *Computational Biology of the Heart*. John Wiley and Sons: Chichester, 1997.
11. Takahashi Y, Usui S, Okazaki T. Range of entrainment of rat circadian rhythms to sinusoidal light-intensity cycles. *AJP-Regulatory, Integrative and Comparative Physiology* May 2000; **278**:R1148–R1156.
12. Filatrella G, Nielson AH, Pederson NF. Analysis of a power grid using a kuramoto-like model. *The European Physical Journal B - Condensed Matter and Complex Systems* 2008; **61**:485–491.
13. Galton I, Towne DA, Rosenberg JJ, Jensen HT. Clock distribution using coupled oscillators. *Proceedings of IEEE ISCAS*, Vol. 3, Atlanta, GA, May 1996; 217–220.
14. O'Mahony F, Yue CP, Horowitz MA, Wong SS. A 10-GHz global clock distribution using coupled standing-wave oscillators. *IEEE Journal of Solid-State Circuits* November 2003; **38**(11):1813–1820.
15. Fradkov AL, Andrievsky B. Synchronization and phase relations in the motion of two-pendulum system. *International Journal of Non-Linear Mechanics* July 2007; **42**:895–901.
16. Kapitaniak M, Czolczynska K, Perlikowska P, Stefanska A, Kapitaniak T. Synchronization of clocks. *Physics Reports* August 2012; **517**:1–69.
17. Koch AJ, Meinhardt H. Biological pattern formation: from basic mechanisms to complex structures. *Reviews of Modern Physics* October 1994; **66**:1481–1507.
18. Kessler DA, Levine H. Pattern formation in dictyostelium via the dynamics of cooperative biological entities. *Physical Review E* December 1993; **48**:4801–4804.
19. Maini PK, Painter KJ, Chab HNP. Spatial pattern formation in chemical and biological systems. *Journal of the Chemical Society-Faraday Transactions* 1997; **93**:3601–3610.
20. Turing AM. The Chemical Basis of Morphogenesis. *Philosophical Transactions of the Royal Society of London. Biological Sciences*, 1952; **237**(641):37–72. Series B.
21. Prigogine I, Lefever R. Symmetry breaking instabilities in dissipative systems II. *Journal of Chemical Physics* 1968; **48**:1695.
22. Lin AL, Hagberg A, Ardelea A, Bertram M, Swinney HL, Meron E. Four-phase patterns in forced oscillator systems. *Physical Review E* 2000; **62**:3790–3798.
23. Lin AL, Bertram M, Martinez K, Swinney HL. Resonant phase patterns in a reaction-diffusion system. *Physical Review Letters* May 2000; **84**:4240–4243.
24. Winfree AT. Spiral waves of chemical activity. *Science* February 1972; **175**(4022):634–636.
25. Winfree AT. Varieties of spiral wave behavior: an experimentalist's approach to the theory of excitable media. *Chaos: An Interdisciplinary Journal of Nonlinear Science* 1991; **1**(3):303–344.
26. Jahnke W, Winfree AT. A Survey of spiral-wave behaviors in the Oregonator model. *International Journal of Bifurcation and Chaos* June 1991; **01**(02):445–466.
27. Keener JP. Spiral waves in the Belousov-Zhabotinskii reaction. *Physica D: Nonlinear Phenomenon* September 1986; **21**:307–324.
28. Winfree A. Biological rhythms and the behavior of populations of coupled oscillators. *Theoretical Biology* 1967; **16**:15–42.
29. Kuramoto Y. *Chemical Oscillations, Waves, and Turbulence*. Springer: Berlin, 1984.
30. Kuramoto Y, Nishikawa I. *Cooperative Dynamics in Complex Physical Systems*. Springer: Berlin, 1989.
31. Bohn A, Garcia-Ojalvo J. Synchronization of coupled biological oscillators under spatially heterogeneous environmental forcing. *Journal of Theoretical Biology* January 2008; **250**:37–47.
32. Lai X, Roychowdhury J. Fast simulation of large networks of nanotechnological and biochemical oscillators for investigating self-organization phenomena. *Proceedings of IEEE ASP-DAC*, Yokohama, Japan, January 2006; 273–278.
33. Strogatz SH. From Kuramoto to Crawford: exploring the onset of synchronization in populations of coupled oscillators. *Elsevier* 2000; **143**:1–20.
34. Matthews PC, Mirollo RE, Strogatz SH. Dynamics of a large system of coupled nonlinear oscillators. *Physica D: Nonlinear Phenomenon* September 1991; **52**:293–331.

35. Neogy A, Roychowdhury J. Analysis and design of sub-harmonically injection locked oscillators. *Proceedings of IEEE DATE*, Grenoble, France., March 2012; 1209–1214.
36. Schiek RL, May EM. Examining tissue differentiation stability through large scale, multi-cellular pathway modeling. *Nanotech 2005*, Anaheim, CA, May 2005; 516–519.
37. Poston T. *Catastrophe Theory and its Applications*. Dover Publications: Dover, 1997.
38. Nagel LW. Spice2: a computer program to simulate semiconductor circuits. *Ph.D. Thesis*, EECS Department, University of California, Berkeley, Electronics Research Laboratory, 1975. Memorandum no. ERL-M520.
39. Demir A, Mehrotra A, Roychowdhury J. Phase noise in oscillators: a unifying theory and numerical methods for characterization. *IEEE Transactions on Circuits and Systems–I: Fundamental Theory and Applications* May 2000; **47**:655–674.
40. Narayan O, Roychowdhury J. Analysing oscillators using multitime PDEs. *IEEE Transactions on Circuits and Systems–I: Fundamental Theory and Applications* July 2003; **50**(7):894–903.
41. Gear CW. *Numerical Initial Value Problems in Ordinary Differential Equations*, Prentice-Hall Series in Automatic Computation. Prentice-Hall: Englewood Cliffs, N.J., 1971.
42. Dahlquist G, Björck A. *Numerical Methods*. Dover: Dover, 2003.
43. Farkas M. *Periodic Motions*. Springer-Verlag: New York, 1994.
44. Demir A, Roychowdhury J. A reliable and efficient procedure for oscillator PPV Computation, with phase noise macromodelling applications. *IEEE Transactions on Computer-Aided Design* February 2003; **22**:188–197.
45. Bhansali P, Srivastava S, Lai X, Roychowdhury J. Comprehensive procedure for fast and accurate coupled oscillator network simulation. *Proceedings of ICCAD*, San Jose, CA., November 2008; 815–820.
46. Roychowdhury J. Hierarchical abstraction of phase response curves of synchronized systems of coupled oscillators, June 2011. ArXiv e-prints.
47. Wen Q, Po MD, Hulme E, Chen S, Liu X, Kwok SW, Gershow M, Leifer AM, Butler V, Fang-Yen C, Kawano T, Schafer WR, Whitesides G, Wyart M, Chklovskii DB, Zhen M, Samuel AD. Proprioceptive coupling within motor neurons drives C.ælegans forward locomotion. *Neuron* 2012; **76**(4):750–761.
48. Chen Z, Iwasaki T. Matrix perturbation analysis for weakly coupled oscillators. *Systems and Control Letter* February 2009; **58**:148–154.
49. Rippard WH, Pufall MR, Kaka S, Silva TJ, Russek SE, Katine JA. Injection locking and phase control of spin transfer nano-oscillators. *Physical Review Letters* August 2005; **95**(6):067203.
50. Zee P. Circadian Rhythms Physiology. *Proceedings of National Sleep Medicine Course*, Westin Tabor Hotel, Denver, CO., August 2007.
51. Katriel G. Synchronization of oscillators coupled through an environment. *Physica D: Nonlinear Phenomenon* November 2008; **237**:2933–2944.
52. Demir A. Floquet theory and non-linear perturbation analysis for oscillators with differential-algebraic equations. *International Journal of Circuit Theory and Applications* Mar/Apr 2000; **28**(2):163–185.
53. Adler R. A study of locking phenomena in oscillators. *Proceedings of the I.R.E. and Waves and Electrons* June 1946; **34**:351–357. Reprinted as [4].